

Towards heralded Ion-Photon entanglement for Quantum Communication

Laboratoire de Matériaux et Phénomènes Quantiques, Université Paris Cité

Paris Physics Master, M1 Internship report, by:

Juan L. Santana González

Supervised by: Sara Ducci & Luca Guidoni

June 28, 2023

Abstract

During my short internship at the *Laboratoire de Matériaux et Phénomènes Quantiques (MPQ)*, I integrated myself in the research environment, studying the research areas of the *Quantum Information and Technologies* group (QITe) and participating in experimental demonstrations. I got specifically involved in the design of a new project that aims to connect two of the activities of the group, Trapped Ions and Non Linear Photonics. It is possible to entangle the quantum state of a confined ion with a spontaneously-emitted photon, making it possible to transmit such state up to large distances through optical fibres. This could be the basis of a Quantum Network that allows for the exchange of quantum information over large distances, or that produces the entanglement between qubits of the same local device. The challenges upon completing this task are numerous and far from easy to solve. The first steps of achieving the ion-photon entanglement necessary to implement this quantum Network involve a study of the needed setup, from optical characterisation and emitted photon collection and analysis, to the integrated devices that can perform wavelength conversion in the single photon regime.

Contents

1	Introduction	1
1.1	The Laboratory	1
1.2	Quantum Communication and Quantum Computation	1
2	Cold trapped Ions	3
2.1	Trapping ions through electrical potentials	3
2.2	Quantum Computation and Communication with the Sr+ Ion	5
3	Photonics	6
3.1	Introduction to non linear photonics	6
3.2	Non linear processes	7
4	Design of the New Experiment	10
4.1	Laser tuning and stabilisation	10
4.2	Collecting entangled photons	14
4.3	Carrying out the frequency conversion	17
5	Conclusion	20
A	Ring Traps	20
B	Producing the ion-photon entanglement	22
C	Manipulation and characterization of optical fibres	25

1 Introduction

1.1 The Laboratory

The *Laboratoire de Laboratoire de Matériaux et Phénomènes Quantiques* (**MPQ**) is located in the Grand Moulin campus, inside the Condorcet building, and belongs to the *Université Paris Cité* physics department. The lab hosts four research groups, with topics ranging from Quantum Technologies to Condensed Matter Physics.

The group which I belonged to is the *Quantum Information and Technologies* group (**QITe**). The group's research consists of three topics with dedicated areas; The trapped ions group, the photonics group and, the theoretical group. During my internship, I worked in the interface between the trapped ions group and the photonics group, in a new project that supposes a deep connection between the two experimental platforms. In the following, I will introduce the main research topics of each group in which I have been involved, and explain some concepts that will be essential to understand the possible development of this new project.

1.2 Quantum Communication and Quantum Computation

After its development at the beginning of the 20th century, Quantum Mechanics has revolutionised and changed the way we see, understand, or manipulate the world around us. It is arguably the most successful scientific theory in the history of humanity, and has led the fastest economic and cultural change that the planet has ever seen. Now, with a deeper knowledge and experience on the

topic, the world moves towards a *Second Quantum Revolution* (SQR) [1], where we discover how to engineer and control quantum systems to obtain precise and desired outcomes, outside of what would be possible simply by nature.

Possibly the most acclaimed technology of the SQR is quantum computation and communication. Quantum Computing (QC) is a concept that has been around since the '80s when scientists (R. Feynman seems to have been the first) realised that there was a problem in the simulation of quantum physics using a classical computer [2, 3]. Since then, many more applications have been discovered, for example, there is proof that a perfect quantum computer could find the prime factors of a big number in a time that scales logarithmically with the size of the number, instead of exponentially as is the case in a classical computer (this algorithm is known as *Shor's algorithm* [4]). This could have a tremendous impact on the world because most of the public key cryptography used for secure data transmission is based on this principle¹. A functioning Quantum Computer could also be used to simulate new molecules [6] to help design new medical drugs [7] or to understand very high-energy quantum systems in order to test cosmological theories [8].

Together with the idea of a Quantum Computer, the natural concept of the *Quantum Network* immediately comes about. A Quantum Network is a system of links connecting many "quantum nodes", that could be the processing cells inside a single quantum computer (very much like it happens in a classical computer) allowing them to scale in qubit number and complexity [9, 10], or quantum storage facilities separated by a great distance. With this last example, we are now referring to the field of Quantum Communication, which encompasses topics like quantum key distribution (which would solve the previously mentioned problem of the present public key distribution) [11, 12], quantum teleportation [13, 14] or the quantum internet [15].

It is under these umbrella terms that the QITe group's research falls under. Trapped Ions is one of the most promising platforms to implement a quantum memory and processor, due to the long coherence time of their electronic states, and because their degrees of freedom are easily manipulable through lasers. There are also many different ways to implement qubits and logic gate computation thanks to the variety of species available in nature. Furthermore, modern traps can be manufactured taking advantage of the already present industry of electronic devices [16, 17]. These traps could be used as the already mentioned quantum nodes of the network. On the other hand, photons represent the perfect system for a "flying" qubit, that would be able to be transmitted over large distances without losing the coherence of the quantum state. Photons have low probability of interaction with the environment, and they can be efficiently transported over long distances through already existent optical fibre networks. Finally, the relationship between the quantum state of an ion and the quantum state of a photon emitted from that ion has been extensively studied [18, 19]. Therefore, trapped ions and photons appear among the possible components for an implementation a real quantum network [20, 21].

However, there is a clear separation between the idea and the realisation, which is far from simple. First of all, the ionic species has to be carefully selected to be a good candidate, not only to perform logic gate quantum computing but also to be able to entangle with a photon in an optimal way to capture such photons and transport the information. Furthermore, the collection of several different wavelengths also increments the complexity of the optical systems, as we will see in this work.

Photons emitted by ions are usually in the visible spectrum of light. This type of light experiences heavy losses inside optical fibres due to absorption and Rayleigh scattering [22]. Because of this, the

¹By the time of this report however, the record for the biggest number factorised by Shor's algorithm is 35, and the results were inconclusive [5]. Rest assured, our credit card information will be safe for still some time.

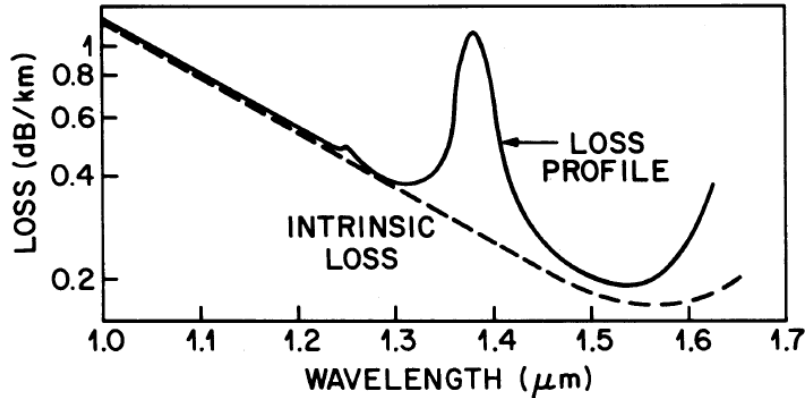


Figure 1: Spectrum of fibre losses. The contribution of Rayleigh scattering is indicated by dashed lines. Adapted from [22]

photons must be converted to the telecommunication wavelength (around $1.5 \mu\text{m}$) without disrupting its quantum state, before being transmitted by long range fibres. This operation is called Quantum Frequency Conversion (QFC), and is in itself a dedicated subject inside the branch of non linear photonics. It was part of my work, to complete a general bibliography on how to perform the QFC with the wavelength 1092nm emitted by the ions, including the methods, materials, and devices that allow for such conversion, and options to implement it efficiently in our specific case. Due to the presence of the Photonic group, experts in the fields of integrated sources of correlated photons and manipulation of photonic quantum states, it is our objective to be able to design and implement our own QFC device adapted to our needs, or at the very least, do it in collaboration with one of the many partners that the MPQ laboratory has.

In the following, I will introduce each topic separately, and discuss what makes them interesting and suitable to achieve a Quantum Network. I will then describe my small part of the project and the steps taken to achieve the goal. Finally, I will describe the challenges yet to come to realise it.

2 Cold trapped Ions

2.1 Trapping ions through electrical potentials

An electrostatic field cannot achieve a potential capable of trapping a charged particle [23]. This is the famous Earnshaw's theorem of electromagnetism, which explains that, if an electrostatic potential is applied between two electrodes, a repulsive force will arise in at least one of the 3 directions of space, and the midpoint between the electrodes will become a saddle point (this is the only possible solution to the Laplace equation). If a trapping electric potential is to be generated, it must be done using both DC and AC fields. The problem was solved in 1958 by the German physicist Wolfgang Paul, who created a way to trap ions inside 3 electrodes by applying a radiofrequency (RF) electric field with a quick oscillation, with an associated time scale much shorter than that of the dynamics induced by the repulsive force [24]. This way, the particle does not have time to escape through the repelling direction and stays trapped in the centre of the trap, effectively describing a harmonic motion [25]. The Paul trap gave birth to the trapped ions research area. The configuration of the

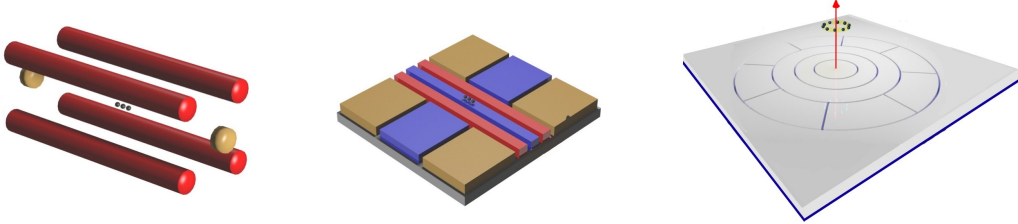


Figure 2: Evolution of the ionic traps. **From left to right**, the first linear Paul trap, the surface trap, and the ring trap (currently used in our setup). The ions are indicated by small spheres. The red arrow in the ring trap only specifies the direction of symmetry but carries no physical meaning. The size of each side (the longer side for the linear trap) is around $100 \mu\text{m}$ for every trap. Images adapted from [25, 29].

trap quickly evolved to allow for the linear trapping of more ions with the application of a confining DC field in one direction, essentially allowing for the trapping of whole 1D ion chains [26], or even the formation of Coulomb crystals [27, 28].

The linear trap was finally refined until all the electrodes could be situated in the same plane [30, 31]. This was the last advance needed for the area to become central in the quantum computation and information topic [32, 33]. Indeed, without electrodes in the middle, the ions, suspended from the electrode plane by 20 to $200 \mu\text{m}$, are very easily accessible through collimated lasers. These lasers can be manipulated outside the chamber and directed towards the ion via free space alignment or through waveguides integrated into the trap [34, 35]. The lasers are of central importance to achieve Doppler cooling of the ions [36] and to perform quantum computation. As a consequence, a trapped ion can be cooled down to the mK [37], and quantum gate operations can be performed with more than 99% fidelity [38, 39].

Another advantage of the trapped ions platform is that it can easily be scaled. To achieve the so called *Quantum supremacy* (this refers to the situation in which a quantum computer can realise an algorithm that a classical computer could only finish in an unacceptable time) the estimated number of needed qubits ranges from a million to a hundred million [40] depending on the application². The trapped ions are a very good candidate as a platform to hold a large number of qubits due to their long coherence time (up to an hour for a single ion [43]) and the high available control over internal degrees of freedom (and hence, over the qubit states). Several implementations of large quantum computers have been proposed for this platform, with a great variety of approaches [9, 10, 20].

At present, the Trapped Ions group has several ongoing experiments with surface linear traps as well as with ring traps. The latter is a new trap design in which the ions are trapped in a circumference, where their angular motion can also be restricted [44]. More information about the ring traps can be found in Annex A.

²However, this number is likely to be reduced after further research, for example with the recent claim from the Canadian company D-Wave of having achieved a complete calculation of quantum dynamics in spin crystals [41] using quantum annealing [42] with only 5000 qubits.

2.2 Quantum Computation and Communication with the Sr+ Ion

Alkaline-earth's atoms are usually chosen due to the simple hydrogenic form of their positive ions, because the neutral atoms possess an s^2 valence orbital, although some other transition metals also share this property and can be implemented in the same way. Many implementations of quantum operations include two species of atoms in the same trap [39, 45]. Normally, an ion with hyperfine structure is chosen to store the qubit information and perform local operations, while the other is used to transmit the information.

The fundamental unit of quantum information is the qubit. A qubit is essentially any quantum system that can be in a superposition of two levels, which will be the quantum analogy for the classic bit 0 & 1, and which has a relaxation time between such levels that is either infinite or much longer than the typical quantum gate operation time [33]. In the Sr ion (see the level scheme in Figure 3), we can implement this system in two ways (these "ways" are called basis):

- Zeeman Qubit: The ground state $5s^2 S_{1/2}$ of the Sr ion has a spin degeneracy that can be lifted by magnetic fields, forming two Zeeman levels of separation $\Delta E/B = g_J\mu_B = 28.0 \text{MHzmT}^{-1}$. These states can form a qubit because the short separation provides a very long-lived upper level, and because the two states can be addressed via RF fields, making it possible to manipulate the state [46]. We will refer to these states as $|^2S_{1/2,m=1/2}\rangle \equiv |\uparrow\rangle$ and $|^2S_{1/2,m=-1/2}\rangle \equiv |\downarrow\rangle$.
- Optical Qubit: Almost all hydrogenic ions have metastable D states. These states are connected to the ground state by a quadrupolar electric transition, which has a long lifetime. Because of this, optical qubits are usually implemented between the $|\downarrow\rangle$ Zeeman state and one of the 6 Zeeman levels in which $D_{5/2}$ splits up. [21, 45, 47]. The name originates from the fact that the transition can be addressed by a 674nm laser (in the visual regime of the spectrum).

The information encoded on such basis can be transmitted via a photon making use of the selection rules of the Zeeman levels. In the dipolar approximation, these transitions between Zeeman levels have to satisfy $\Delta m = -1, 0, 1$, hence limiting the variation in the magnetic quantum number m . Due to the conservation of angular momentum, the emitted (or absorbed) photons need to have a very specific polarization. As an example that we can see in Figure 3, the excited state $|P_{1/2,-1/2}\rangle$ is connected to the two states of the basis $|\uparrow\rangle$ and $|\downarrow\rangle$. Because the ion results in a linear combination of this basis after the decay (given by the Clebsch-Gordan coefficients), and the polarization state of the photon is directly dependent on the final state of the ion, the ion-photon system is entangled. This simple example is used in many previous implementations of ion-photon entanglement in Sr^+ [45, 47].

In our case however, we wish to generate entangled photons at 1092nm, because their conversion to the telecom band should be easier. This means that our entanglement procedure will be slightly different, starting from the fact that we need to use the $|P_{1/2,-1/2}\rangle \rightarrow |D_{3/2}\rangle$ transition to produce the entangled states, and taking into account that this is not the preferred transition, it only represents 5.8% of the decays. This carries many complications and subtleties. The Sr ion also presents many benefits in terms of its photoionization scheme and the way we can implement Doppler cooling thanks to its level scheme. A full description of the entanglement sequence is far too complex for the purpose of the main text of this report. However, a more in-depth explanation of the can be found in the Annex B, as well as a deeper explanation of the Sr strong points.

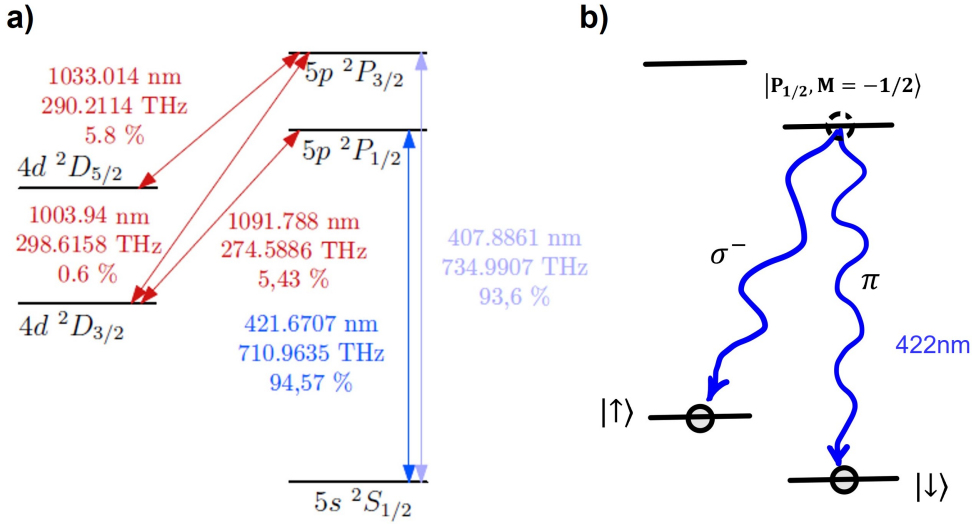


Figure 3: a), $^{88}\text{Sr}^+$ level scheme, without Zeeman splitting, adapted from [48]. b), A possible entanglement sequence. The ion decays to the ground state via emission of a left-handed circular polarized (σ^-) photon or a photon in a linear combination of both circular polarizations (π), forming the Zeeman basis. The final state of the ion is a superposition of both states given by the Clebsch-Gordan, producing a final entangled state: $|\psi\rangle = 1/\sqrt{3}|\downarrow, \pi\rangle - \sqrt{2}/\sqrt{3}|\uparrow, \sigma^-\rangle$

3 Photonics

3.1 Introduction to non linear photonics

Photons are the paradigm of quantum phenomena. Indeed, they have been used to demonstrate quantum behaviour like no other system, as it was made clear by the black body spectrum of radiation described by Planck [49], or by the demonstration of the non-local behaviour of quantum mechanics [50], although maybe the most impacting application is the laser. These particles are weakly interacting, very fast (as fast as physics allows) and very easy to generate. They can be transported for km in complex fibre networks that are already designed and implemented throughout the world.

The implementation of a qubit in a photon is straightforward and far from unique. Information can be encoded in any of the degrees of freedom of the photon, like its polarization [51, 52] or its energy [53]. It can also be encoded on external degrees of freedom, like spatial modes [54] or temporal modes [55]. Furthermore, there exist many apparatus capable of manipulating photonic states down to the single photon regime. For example, only with phase shifters and beamsplitters, one can perform any optical operation in a photonic qubit [56].

However, the most important thing for our application is that photons can interact inside a non-linear media. Usually, the polarization of a material is proportional to the external electric field. This means that the material creates an internal electric field with the same frequency as the external field. Down to the single photon level, the consequence is that the photons that scatter inside the

material does not suffer any change of its state, apart from wavevector orientation³. Nonetheless, when the applied electric field is strong enough, all materials behave in a non linear way, that can be described by:

$$P = \epsilon_0 [\chi^{(1)} E + \chi^{(2)} E^2 + \chi^{(3)} E^3 + \mathcal{O}(E^4)]$$

Where we have included second and third order effects. Here, the susceptibility must be thought of as a tensor of second and third rank for the second and third order polarization respectively. It is now clear that, if the external field is composed of more than one frequency, the response of the material will have several different components with different frequencies given by conservation of energy and momentum. We will explore some of these options and their application in the following section.

3.2 Non linear processes

The lowest order non linear process we can think of involves second order polarization. This polarization will in principle dominate over the third order (for non-centrosymmetric materials, as we will see), and will produce interactions between three fields. This is the reason why sometimes it is called Three Wave Mixing (TWM). Let us suppose that the external field is a classical wave with 2 frequency components:

$$\mathbf{E} = \frac{1}{2} (\mathbf{E}_1 e^{-i\omega_1 t} + \mathbf{E}_2 e^{-i\omega_2 t} + c.c) \quad (1)$$

Therefore, we can expand the second order polarization in all of its terms:

$$\begin{aligned} P^{(2)} = \epsilon_0 \chi^{(2)} \mathbf{E} \mathbf{E} &= \epsilon_0 \chi^{(2)} [\mathbf{E}_1^2 e^{-i2\omega_1 t} + \mathbf{E}_2^2 e^{-i2\omega_2 t} + 2\mathbf{E}_1 \mathbf{E}_2^* e^{i(\omega_2 - \omega_1)t} \\ &\quad + 2\mathbf{E}_1 \mathbf{E}_2 e^{-i(\omega_2 + \omega_1)t} + c.c] + 2\epsilon_0 \chi^{(2)} [\mathbf{E}_1 \mathbf{E}_1^* + \mathbf{E}_2 \mathbf{E}_2^*] \end{aligned} \quad (2)$$

As we can see, now we have several terms related to a third involved frequency and two non-oscillating terms relating to optical rectification of the external field. The third frequency can have the following values:

$$\omega_3 = \begin{cases} 2\omega_1 & (\text{SHG}) \\ 2\omega_2 & (\text{SHG}) \\ \omega_1 + \omega_2 & (\text{SFG}) \\ \omega_1 - \omega_2 & (\text{DFG}) \end{cases}$$

The two first are related to the process of second harmonic generation (SHG), in which two photons with the same frequency are annihilated producing one single photon with double frequency. SHG can be seen as a special case of Sum Frequency Generation (SFG), where now the two annihilated photons have different frequencies and generate a frequency equal to the sum of both. The last one is Difference Frequency Generation (DFG), in which now the generated photon has a frequency given by the difference of the external wavelengths. In order to conserve energy, 2 photons of the lowest incoming frequency must be generated, and for this reason, this process is also known as optical parametric amplification (OPA). Normally, only one of these processes can happen efficiently, because they require very distinct phase matching conditions⁴ that are also sensible to polarization.

³In this simple consideration, we have neglected usual effects like absorption, inelastic scattering or birefringence, among others. We limit our discussion to the transparency region of the material.

⁴The conservation of energy is not the only law that determines the conversion efficiency. The conservation of momentum is far from guaranteed and the system must be engineered to achieve it. If the conditions are met for this conservation law to apply we say that we have achieved Phase-Matching. Its description escapes the scope of this report but can be seen in [22, 58].

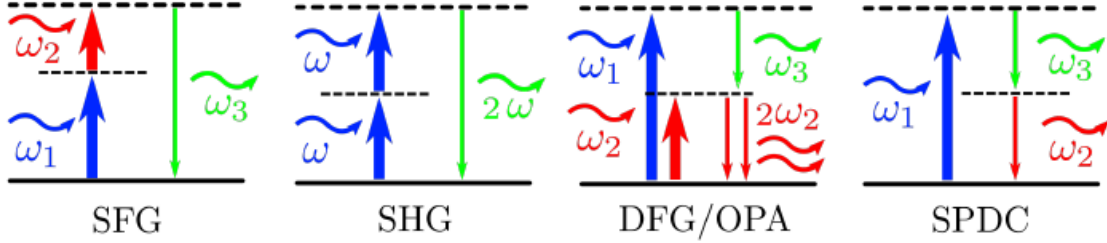


Figure 4: Energy diagrams of the TWM interactions. Adapted from [57]

They also depend on the $\chi^{(2)}$ coefficient, which is a rank two tensor dependent on the crystalline structure. Therefore, by choosing an orientation between the crystal and the incoming fields, one can normally choose the preferred interaction. A complete description of this phenomenon can be found all over in literature in many forms, for example in terms of the fields' amplitudes or based on quantum mechanical formulation [58].

It is easy to see that, for our application of frequency conversion, SFG and DFG are very attractive. In practice, a weak "signal" field will interact with a strong classical pump field that could be generated with a CW laser, to produce a converted "idler" field. In the undepleted approximation of the pump beam, it can be considered as a purely classical field and we can write the Hamiltonian of the interaction:

$$\hat{H} = i\hbar|\epsilon|(e^{i\phi}\hat{a}_i^\dagger\hat{a}_s - e^{-i\phi}\hat{a}_s^\dagger\hat{a}_i)$$

Here, $|\epsilon|$ is a coupling constant proportional to the pump beam power, and ϕ is its phase. In the Heisenberg's picture, the evolution of the creation operators can be written [59]:

$$\hat{a}_i^\dagger(\tau) = e^{-i\phi} \sin(|\epsilon|\tau)\hat{a}_s^\dagger(0) + \cos(|\epsilon|\tau)\hat{a}_i^\dagger(0)$$

From here, we can see that, by adjusting the travelling time of the wave in the material τ , and the pump characteristics, a full conversion is realised for $|\epsilon|\tau = \pi/2$.

Finally, it is worth noting a special case of DFG called Spontaneous Parametric Down Conversion (SPDC), as it will be very important in noise considerations of TWM QFC. It happens when a single pump photon of frequency ω_1 is "fissioned" into two photons of frequency ω_2 and ω_3 , and can be used to produce colour or polarization entangled pairs of photons [60, 61]. This is actually one of the main lines of research of the Photonics group at QITE, therefore it will become one of the building blocks of the experiment in the future. However, it was not the subject of my recent internship, so I will not investigate this topic any further on this occasion.

In materials that show inversion symmetry, the second order susceptibility $\chi^{(2)}$ becomes exactly zero⁵, which means that the next non-linear term is the third order. For an external e.m. wave

⁵Also known as centrosymmetric crystals, these are crystals which are symmetric with respect to inversion around a certain point of the lattice. 11 of the 32 classes of crystal show this property. In a lossless medium, inverting the electrical field must mean inverting the polarization vector, due to inversion symmetry [58]. Therefore :

$$-P^{(2)} = \epsilon_0\chi^{(2)}(-E)^2 = \epsilon_0\chi^{(2)}E^2 = P^{(2)} \iff \chi^{(2)} = 0$$

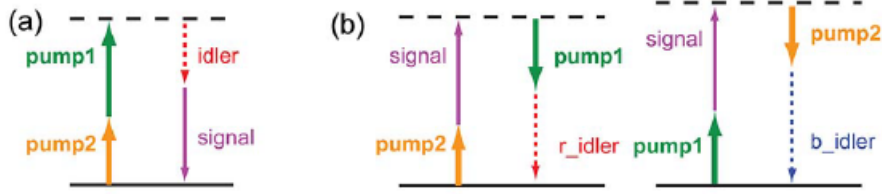


Figure 5: Field Diagrams for **a)** Parametric Amplification, and **b)** Bragg Scattering. Here, we see the reason why two idlers are generated. Having pump 1 in the signal band and pump 2 in the idler band, there are two ways to conserve the energy, either the energy separation between pumps is the same as between signal and idler (which generates ω^+) or the separation between the first pump and the signal is the same as for the second pump and the idler (ω^-). In the diagram, b_{idler} and r_{idler} refer to the blue shifted (more energetic) and red shifted (less energetic) idler fields. The diagram should not be seen as an energy diagram but rather as a created-annihilated photon representation. Adapted from [69].

made from three distinct frequencies:

$$\mathbf{E} = \frac{1}{2}(\mathbf{E}_1 e^{-i\omega_1 t}) + \mathbf{E}_2 e^{-i\omega_2 t} + \mathbf{E}_3 e^{-i\omega_3 t} + c.c \quad (3)$$

The non linear polarization is now proportional to the cube of the external field. This produces 44 different components for the polarization, characterised by all the possible combinations of the three frequencies, and also some non oscillating terms. These non oscillating terms are responsible for the processes of self-phase (SPM) and cross-phase modulation (XPM) and will not be treated here (see ref. [22] for an extensive description). All the oscillating combinations are very well described in ref. [58], and allow for a wide range of applications, from which fibre optical parametric amplifiers (FOPAs), and frequency converters stand out [22, 62]. FOPAs are based on the principle of parametric amplification of the weak signal field upon interaction of two undepleted pump beams (also resulting in the creation of a weak fourth field) [63–65]. In this case, the practical implementation needs two strong undepleted pump beams. As a consequence, and differently from TWM processes, two idlers can be produced instead of one. We are only interested here in the processes that are useful for frequency conversion in the low photon regime, with the idler field generated at frequency $\omega_4 = \omega_3 \pm |\omega_1 - \omega_2|$. These can be divided into three types [66]: modulation interaction, phase conjugation and Bragg scattering.

Modulation interaction only produces intraband conversion, i.e. both signal and idler photons are very close in frequency. Phase conjugation consists of the annihilation of two pump beam photons and the creation of a signal and idler photons whose fields are complex conjugates (hence the name phase conjugation), and its main application is to compensate light dispersion in optical communication systems. [67, 68]. Both processes involve the creation of low populated field, which produces vacuum amplification that increases the noise in the signal. Bragg scattering (BS-FWM) however, involves the annihilation of a pump and a weak signal photon to create a pump and weak idler photon, essentially transferring the power of the signal field to the idler field. This provides a much wider and tunable transformation band with low noise conversion, which is desirable for QFC [70]. This is the reason why all QFC implementations utilise Bragg Scattering.

In Bragg Scattering, the pumps are located at distant bands, providing long-distance conversion. However, due to energy conservation, two idlers can be formed at symmetric distances from the

pump in its band. Afterwards, we could select one of them with a narrowband filter (that we would already use to filter the second pump) accepting some loss⁶ or even using another FWM device to carry an intraband frequency conversion (here, in-fibre conversion could become useful).

4 Design of the New Experiment

4.1 Laser tuning and stabilisation

The first fundamental step to perform the experiment is to be able to stabilise and precisely manipulate the coherent light that interacts with the atom, whatever its purpose may be. This avoids unwanted fluctuations in intensity and wavelength that can cause the ions to escape, failures in the entanglement cycles or heating of the ions.

All the experiments on the Trapped Ions group utilise the same tunable *Toptica DL100* laser diode and method of stabilisation. These tunable lasers work under the principle of an extended cavity. In the principal laser cavity, the laser works normally and emits in some mode of the Fabry-Perot spectrum "selected" by the gain of such cavity, in our case, the central wavelength is 421nm. At the output, a grating is located at a non-fixed distance, which works as a mirror and as a diffractor at the same time. The bigger (smaller) portion of the laser beam is reflected out of the cavity if the light is vertically (horizontally) polarized⁷. However, the rest of the light is coupled back into the first cavity, and the system is now a cavity inside of another cavity (this concept is called an *extended cavity*). This second cavity produces new Fabry-Perot peaks to appear, depending on the distance between the exit of the first cavity and the grating. By carefully modifying this distance with a piezoelectric one can effectively choose the wavelength being emitted from the overall laser. During my internship, a malfunctioning grating caused a severe lack of power in one of the 422nm laser and the experiment was not able to run according to expectations. A new grating was ordered and installed, and several characterisations were carried out to ensure than the problem no longer existed. The losses in the new grating were measured to be around 7% for the vertical polarization, quite better than the 19% of the old one. Another noticeable difference is that the new grating only diffracted around 12% of the light back to the primary cavity, while the old one diffracted a quite larger part, around 60%. The new grating with its differences proved to be much more efficient than the old one, as can be seen in Figure 6. The Intensity-Power curve is important to understand the behaviour of our laser, and where are the limits in current and power, in order not to damage any of the laser components. With our new grating, we achieve 10.3mW of power for 35mA of current intensity, which is unexpectedly high for a laser diode. Using specifications from the distributor, we estimated a rupture current of 60mA approximately, which should never be reached.

Once the laser exits the grating, one is still not sure that it has the correct wavelength. We would want to be able to quickly change the parameters of the laser through a PID feedback controller if we detect such fluctuations, to maintain a stabilised beam during the measurement.

This stabilisation is implemented with the principle of saturated absorption. The laser is aligned in some axis with a counter-propagating high intensity pump laser⁸, inside a medium of a neutral Rubidium (Rb) vapour (see Figure 9). We make use of the fact that ⁸⁵Rb has a natural transition

⁶This would not represent such a dramatic measure as it seems, because one of the idlers is almost always much less efficient than the other, especially when the idler-pump distance increases (see [71, 72]).

⁷The difference between polarizations is expected because the grating causes polarization-depending diffraction due to the orientation of the grating layers.

⁸In our case, this pump laser is actually our own laser. The high intensity beam traversing the Rb vapour is back reflected, attenuated and its polarization rotated by 90°. The reinjected beam serves as the probe beam, that will enter the photodiode (D1) and be the signal for stabilisation.

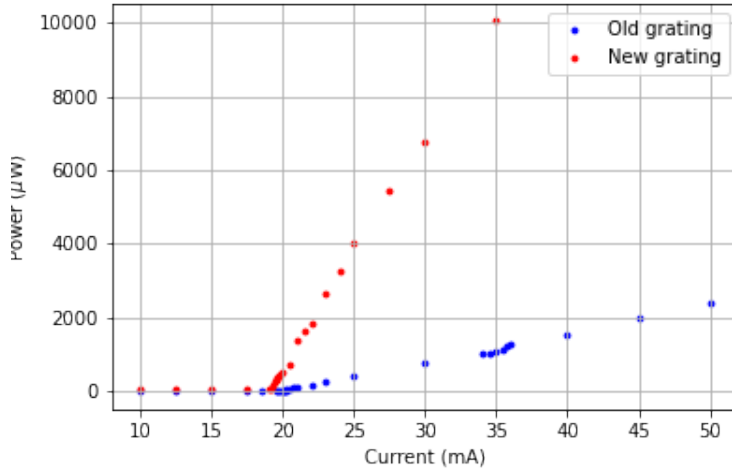


Figure 6: Comparison of the functioning curves of the laser with the old and new grating. The curves present a very small slope given by fluorescence at the beginning, and then they produce laser light whose power increase linearly. The increase is not perfectly linear due to mode jumps of the laser diode cavity.

$|5s^2 S_{1/2}, F = 2\rangle \rightarrow |6p P_{1/2}, F = 3\rangle$ only separated by 440 MHz from our desired Sr+ transition [73]. The atoms in the vapour follow a Gaussian velocity distribution given by the 1-dimensional Maxwell-Boltzmann distribution in the axis of the collimated beams. The pump beam is tuned to excite the atoms with zero velocity (which corresponds to the highest population) up to saturation, while leaving the rest of the atoms approximately unaffected, as their transition is shifted due to Doppler effect. Then, sweeping through the wavelengths of the laser, we can observe a peak in the transmittance at the saturated wavelength, because these atoms can no longer be excited. Since we know with precision the wavelength of our beam, we can lock the PID to this peak, essentially fixing the wavelength of the laser as we want.

The accuracy of this lock can be further increased using the fact that the 422nm excitation is between the ground state of the Rb and a $P_{1/2}$ state that has a hyperfine structure. One would then expect to obtain 2 peaks of transmittance inside the gaussian shaped absorption curve, but 3 are observed instead. This seemingly paradoxical peak appears because, for certain atomic population, the saturated transition of the higher hyperfine level is Doppler shifted to lower energies when moving in the same direction as the pump beam. At the same time, the lower energy hyperfine transition is Doppler shifted to higher energies because the atom is moving contrary to the laser beam. When the velocity is such that these shifted transitions coincide for the same energy, a third peak in transmittance appears exactly as if there was another hyperfine level in the middle of the real ones. This effect is known as crossover and affects all hyperfine structures.

The locking interface essentially modulates the current and the piezoelectrics in the grating of the laser to sweep among the available laser wavelengths. Observing the spectrum coming from a photodiode (D1 in Figure 9), we can observe the gaussian peaks of absorption of the two hyperfine levels of the state $S_{1/2}$ of Rubidium. If we sweep around a narrow region at the bottom of the band, we can see the peaks of transmittance referring to the crossover effect. The distance between the

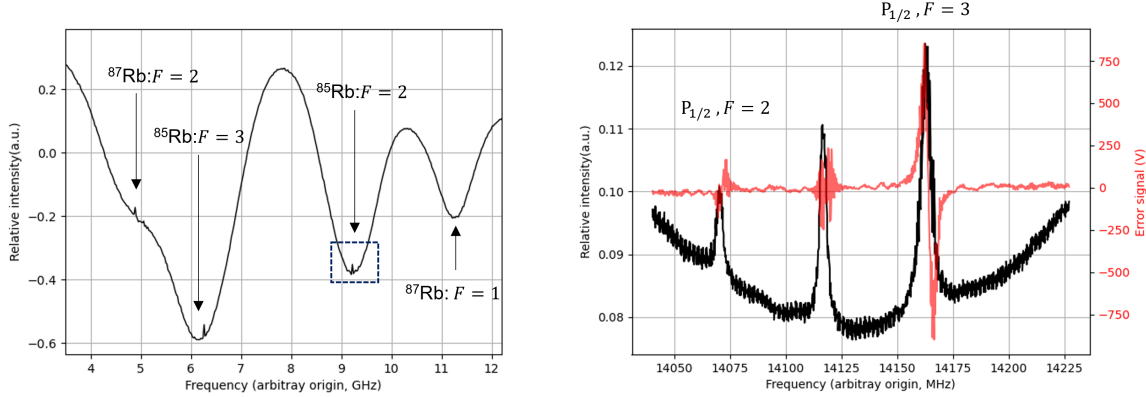


Figure 7: Signal on the photodiode D1. On the **left**, the gaussian-shaped Doppler absorption lines for the transition $|S_{1/2}\rangle \rightarrow |P_{1/2}\rangle$ for both isotopes ^{87}Rb and ^{85}Rb . Here, the hyperfine level from which the transition occurs is designated by F [73]. The separation between the two hyperfine levels of ^{85}Rb is 3035.7 MHz, which was used to scale the x axis [74]. On the **right**, zoom in at the indicated peak of interest. The outer peaks refer to the transitions $|S_{1/2}, F = 2\rangle \rightarrow |P_{1/2}, F = 2\rangle$ and $|S_{1/2}, F = 2\rangle \rightarrow |P_{1/2}, F = 3\rangle$, as indicated, while the centred peak is the crossover explained in the main text. The distance within peaks is 58.7 MHz approximately. The red curve is the error signal that drives the PID response and resembles the derivative of the signal at the peaks.

outer peaks is approximately 117MHz, corresponding to the separation between the $P_{1/2}$ hyperfine levels. The width of the peak is directly related to the relaxation time of this excited state and is approximately 6 MHz. This information also allows to convert the signal to MHz, which is coming from the piezoelectrics in Volts. Once the signal is on the screen, the Toptica autolock system features two PID's⁹ that must be finely tuned for every laser, in order to ensure the most stable lock possible. This is very important because the width of the $S_{1/2} \rightarrow P_{1/2}$ transition in ^{88}Sr is only 21 MHz.

The PID's response needs to be based on a feedback signal that indicates how quickly changes must be imposed in the system and how. Such an "error" signal is generated by a modulation in a magnetic field present in the saturated absorption chamber. The magnetic field oscillates with a modulation that we select, producing small shifts in the levels by Zeeman effect. This produces the peaks to oscillate around a certain central frequency where we want to lock. By demodulating such variation, the error signal is obtained and has essentially the form of the derivative of the photodiode signal. This very clever way of obtaining the behaviour of the laser allows the PIDs to attach to a certain frequency and stabilise the laser (red curve in Figure 7.right).

This is not the last word to be said in terms of laser stabilisation. The change in the grating caused that all the PID parameters had to be adjusted again, and the question that remains would be, how can we be sure that the frequency is actually locked? The answer to this question depends on having a referential stable laser.

The most straightforward way is to make the beam to copropagate with a stable laser and measure the interference. This is shown in Figure 8, when the laser is made to coincide in a beamsplitter

⁹One for fast modulation of the current, which critically changes the power and frequency of the laser, and one slow for the piezoelectrics, which can sweep slowly a small section of the spectrum

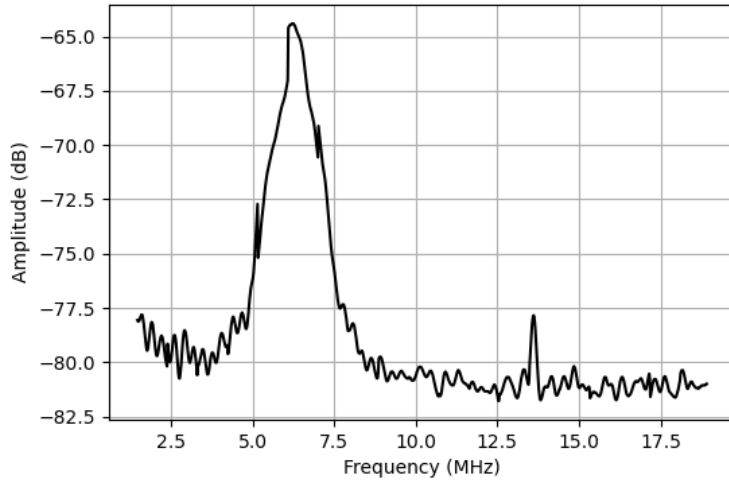


Figure 8: Signal on the spectrum analyser. A beat note is located around 6.15MHz and has a half-peak width of 2MHz. This allows us to have a notion of the actual wavelength (provided that at least one of the two lasers is stabilised) and the width of our laser.

with another well stabilised laser. This reference laser is stabilised by the same principle, but has a small frequency shift given by an acusto-optical modulator (AOM), as we will explain later. Making the beams coincide in a photodiode (D2), we can then measure this spectrum of interference, where we should observe a single peak around the difference in wavelength. Consider the AOM is set to $\delta = 127\text{MHz}$, and with the reference beam locked in the middle peak, it has a frequency of $\omega_0 + \delta$, where ω_0 is the frequency of the central peak and δ is the AOM shift. Now we lock our laser in the right-most peak. This way, it will have a frequency $\omega_0 + \Delta$, where Δ is the distance between peaks. Once the lasers interfere, they will then have a difference in wavelength $\Delta - \delta/2$ [48]. In our case, we observe an interpeak distance $\Delta = 58\text{ MHz}$, and therefore we have approximately 5 MHz of separation, consistent with the observed peak in Figure 8.

Separately, the frequency stabilisation of the IR lasers of 1092, 1033 and 1003 nm is realised in a resonating cavity, using the already stable 422nm laser as a reference.

The last step in the manipulation of the laser is to couple it to an acusto-optical modulator (AOM). An AOM is a device which produces sound waves in a crystal at some controllable radiofrequency (RF). The sound wave propagates with some angle with respect to the direction of the laser, providing a (time and spatial) periodic grating where the laser is diffracted. It has many applications, for example, it is able to switch off the laser completely in a timescale of nanoseconds, which is very important in logic gate operation. More importantly, it provides further tuning of the wavelength, as the diffracted beam is frequency-shifted depending on the RF frequency. With this final step, the laser can be stabilised around the wanted wavelength up to fluctuations of the order of 2 MHz. After the coupling in the AOM, the first order of diffraction is optimised and selected through a diaphragm. The light is then reflected and reinjected into the AOM where it gets diffracted for a second time. We place $\lambda/4$ waveplates to rotate the polarization of light to be able to pass through the previous beamsplitter without losing light. Finally, the order 1 of diffraction is again selected and coupled into a fibre, ready to go to the experiments. Notice that we separate the laser into two

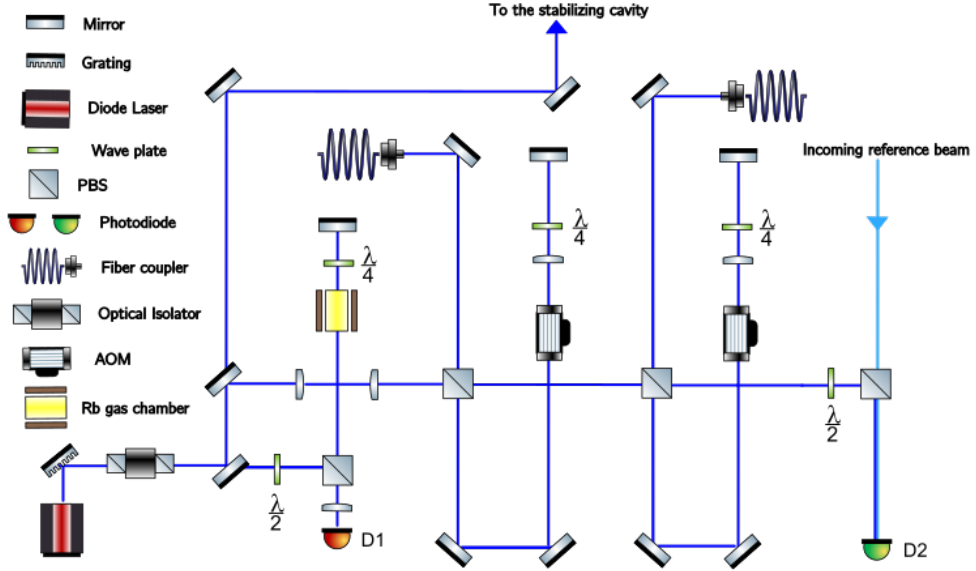


Figure 9: Optical Setup of the stabilisation table. The laser is separated into two different AOM lines that are coupled to independent optic fibres. This allows for independent modification of the wavelength and, therefore, for different applications of the same laser. The incoming reference beam comes from a different stabilization setup on the same table which will not be addressed here.

different AOM lines, producing two independently tunable beams that can be used separately in the experiment.

As an analysis of losses, the coupling to the fibres were of 25% and 60% of the light respectively. The coupling is considered poor below 50%, therefore our coupling to the first fibre can be considerably improved. Considering the overall loss of the optic table added to the losses in the insertion to the vacuum chamber, the final power for each laser is of the order of 50-70 μW , far more than needed for the experiment¹⁰.

4.2 Collecting entangled photons

After the laser stabilisation, the entanglement sequence begins and the ion emits the entangled 1092nm photons and the 422nm transition photons in all directions of space. The trap and the ions are located inside a vacuum chamber and are addressed by the lasers through lateral windows. On the top window of the vacuum chamber, a high numerical aperture (NA) objective captures part of the photons depending on the solid angle that the objective covers (See Figure 10).

A central part of my internship was based on the design of a new collection system. For the previous experiment, it was only possible to collect the 422nm (blue) photons emitted by the ion. They were captured by a special objective designed for such wavelength and dispatched towards a camera or

¹⁰Indeed, the π pulse associated with the Rabi frequency calculated for this power has a duration of around 7ns, which is much less than the time that the AOM takes to shut the lasers. Therefore, we need a longer Rabi frequency (less power) in order to be able to implement a usable sequence (see Annex).

a photo-multiplier (PM). This allowed imaging of the trapped ions and to perform quantum state readouts. In the new experiment, this type of collection is also desired, while we need to also capture the 1092nm (IR) photons to analyse them separately. The solution was to include a shortpass dichroic mirror¹¹ after the objective to separate the two wavelengths into different modules. By choosing a shortpass filter, we facilitate the coupling (it is much more convenient from the point of view of the physical arrangement of the setup) and we ensure minimum modifications in the polarization state of the entangled photon due to reflection. In the IR module, we couple the IR light to a fibre, that could be directed towards a quantum state analyser or to the QFC device. The blue light maintains the same options as before, so we do not lose any information.

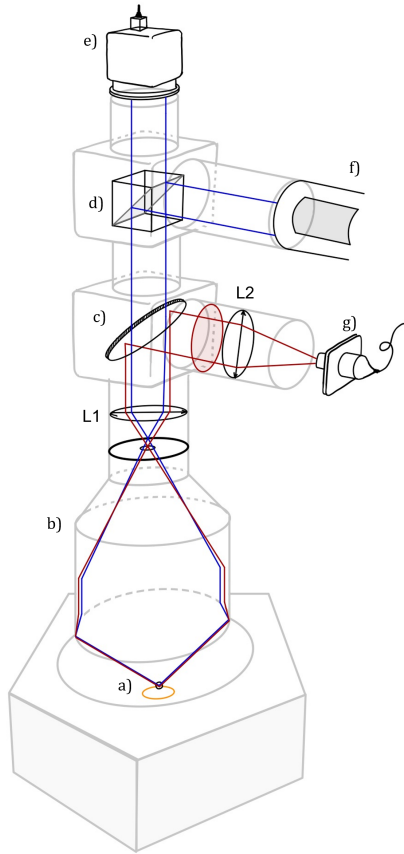


Figure 10: Setup for the collection of photons from the trap (yellow ring at the bottom) explained in section 4.2. The ion **a**) emits photons that are collected in the objective **b**). The post-image of the pinhole is collimated by a short focal length lens L1, and the different wavelengths are separated by a dichroic mirror **c**). The IR (red lines) photons are refocused by a long focal length lens L2 and coupled to a fibre **g**). The blue light (blue line) passes through another nexus where is divided by a non polarizing beamsplitter **d**) to be analysed simultaneously in a photomultiplier **f**) and imaged in a camera **e**).

¹¹The chosen dichroic mirror for the setup was the model 69209 centred at 850nm from *EdmundOptics*

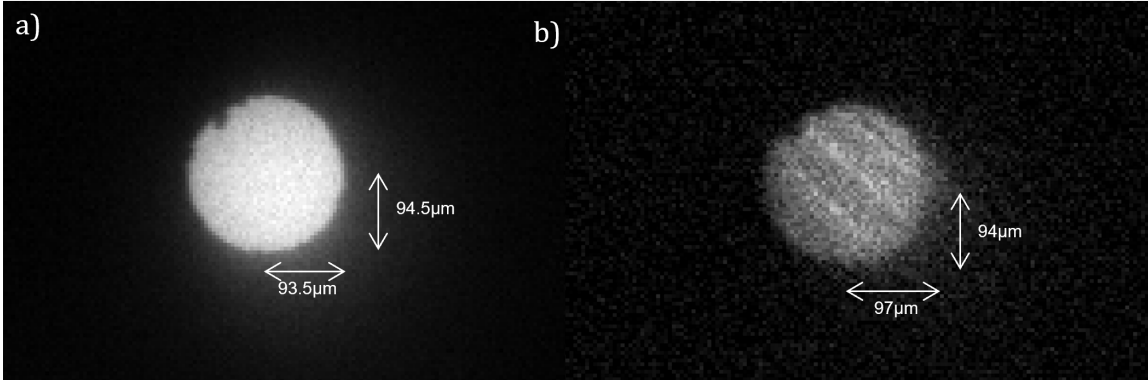


Figure 11: Comparison of the image of a pinhole imaged by light with a) 422nm and b) 1092nm. As it can be seen, the blue light images much better because the shorter wavelength can resolve better the image's details (notice the imperfection of the pinhole in the top-left, for example). The aberration can be observed in the horizontal axis, where the 1092nm light tends to elongate the object. The images are focused at distances which differ by 0.9mm approximately

In order to reduce costs, we analysed the behaviour of the objective concerning to the IR light to see if there were critical differences with the blue light that it was designed to perform on. Our interest was specially directed towards changes in the focal length (chromatic aberration) and losses. To measure the change in the focal length, we built a simple optical setup in which the light exiting a fibre was collected by a set of two lenses and later focused on a pinhole. Then, the objective collected the light filtered by the pinhole and imaged it on a camera at a known distance. Our objective was to measure the difference in distance at which the pinhole image was formed in the camera for the two wavelengths, as well as the shape deformation of the image caused by aberrations. The two images can be seen in Figure 11. The distance of focal length between both images was measured to be 0.889 ± 0.09 mm, which is quite large. We also measured the losses of the objective to be approximately 2.4dB (around 40%) when the incident light was parallel, and rapidly increasing losses for larger angles of incidence up to complete loss at around 30° . In principle, this is not a limiting problem because the polar angle that the objective covers is 22.94° . Making a linear regression to the Loss-Incident Angle curve, we obtain a rate of loss of 2.898dB/cm^{12} , which allows us to calculate a total integrated loss of 6.93dB for the IR light in our objective. Our calculations are actually in line with the specifications provided by the manufacturer (Thorlabs) provided that we can extrapolate linearly from their results, which predict 32.27% of losses for a parallel beam, and a 1.1mm difference in focal length. No specifications are made for angle-dependent variation of losses from their part.

Our results question the possibility to employ our current objective, which is a compound lens object of diameter $\varnothing 5.08\text{cm}$ (2 inches) and an (intended) focal length of 6cm for both frontal and rear lenses. One key point is the location of the pinhole that reproduces that image of the ion after the objective. Due to the difference in focal lengths, centring the pinhole on the focal point for the IR light (closer to the lens) will make us lose around 78% of the blue light, for a pinhole of diameter $\varnothing 150\mu\text{m}$. Here, we have also assumed that the focal lengths for the 422nm light are the same for both lenses of the objective, around 6cm, so the focal point for the IR light is approximately at 5.91 cm of the back lens. This allows us to calculate a collimating angle of 23.26° for the IR light, while

¹²This is the extra amount of light that we lose when we increment 1cm the objective radius exposed to it.

for the blue light is the 22.94° previously mentioned. In order to not lose any blue light, we would need a pinhole of approximately $760\mu\text{m}$. This is not possible because a fine pinhole is needed to reduce the background counts of the photomultiplier as much as possible. Possibly, the best option is to locate the pinhole in the middle segment of both focal points, at the intersection of both rays, in a way that preserves maximally all light and reduces the radius of the pinhole up to a limit of $190\mu\text{m}$ approximately. This position is exactly at 0.35mm of the IR focal point. Precision in the setup mounting will be crucial.

Once the light passes through the pinhole, it needs to be refocused into a parallel beam, before it passes through the dichroic mirror. The maximum focal length of this (L1) lens is 2.95 cm to affect the two beams. In the dichroic filter, the blue light passes through with an efficiency of 85% and gets divided in a non-polarizing beamsplitter to be analysed in both, the camera and the photomultiplier. The IR light, on the other hand, needs to be filtered with a narrow filter around 1092nm to prevent any noise photons coming from the surroundings or the blue beam. The filter will surely introduce aberrations that should be corrected before the light enters the fibre, as well as some losses due to imperfect diffraction.

The last step is to couple the beam with the PM980-XP fibre (Thorlabs). This model has a core diameter of $5.5\ \mu\text{m}$ and a NA of 0.12 . This corresponds to a maximum coupling angle of around 7° . Taking into account that our mounts can hold a $\varnothing 2.54\text{cm}$ lens (L2), it has to have a minimum focal length of 10.51cm . Producing this coupling is not easy either. To help with this task, the fibre will be mounted into a 3 axis stage that allows for delicate movement in two spatial directions and an angle. This would allow us to couple light with an efficiency of at least 50% .

This setup for the collection of entangled photons might work but is fundamentally limited by the saturated emission of the entangled 1092nm photons. A study of the possible photons per second collected needs to take into account all our losses, the solid angle collection, and the rate of generation from the ion. This can be found in Annex B

4.3 Carrying out the frequency conversion

Non Linear crystals are a well studied topic since the invention of the laser, which allowed the coherent manipulation of the Three-Wave-Mixing (TWM) and Four-Wave-Mixing (FWM) processes described before. As a consequence, there are several options to choose from, if one wants to implement a Quantum Frequency Conversion (QFC) device in a setup. One of the important tasks while designing the new experiment is to choose the desired implementation of QFC in terms of fabrication and characterisation options.

By far the better established material to carry on the QFC is Lithium Niobate (LiNO_3) with a periodically polling to implement quasi-phase matching (QPM). The nomenclature used for the material is then PPLN. LN has a high nonlinear coefficient of $d_{33} = 27\text{pm/V}$ and has been heavily used in the industry of telecommunications for decades. It can be produced in waveguides, improving the propagation properties and conversion efficiency, or in bulk for better power handling. There is a great offer of commercial PPLN chips available. QFC has been demonstrated with this material several times with many different configurations [59, 75–82], therefore making it a good candidate for initial tests of the setup. In terms of the efficiency of the conversion, it is arguably the best option, achieving in some instances up to 90% internal efficiency and 41% external efficiency [78]. Another option is Periodically Polled Potassium Tytanil Phosphate (PPKTP) [83]. PPKTP has better resistance to power damage and greater thickness, although it has a smaller nonlinear coefficient than PPLN ($d_{33} = 17\text{pm/V}$) [84]. There have been studies suggesting that bulk PPKTP can be periodically polled with higher quality than PPLN [85–87], and some very recent demonstrations reporting lower levels of noise for a similar external conversion efficiency [88].

Although second order processes in periodically polled materials seem to be the preferable option, there also exist many centrosymmetric materials that can produce QFC through FWM processes. The topic has been extensively studied theoretically for several different options to produce such processes through microresonators [89, 90], in fibres [66, 70] or through adiabatic FWM [91]. Most of them are interesting because they can be implemented in chips and waveguides, which are very convenient to design easy-to-scale and mass-produced devices. For example, efficiencies of 60% have been demonstrated using Bragg scattering in microring resonators of Si_3N_4 [71]. Bragg scattering is the most usual way to perform QFC, due to the low noise level¹³ and large conversion bandwidth. For quantum communication processes, microrings and AlGaAs waveguides seem to be the path to follow. In-fibre FWM is very convenient, but its range of conversion is quite poor (in the order of tenths of nm [92]), and to increase such range, a lot of distance is required (of the order of km [93]). Microrings also have great theoretical support [94], as well as a long range conversion provided that each pump is located on each band of the conversion.

Integrated devices take advantage of the huge semiconductor industry, whose clean-room fabrication has no competitor in quality and efficiency. Therefore, Lithium Niobate On Insulator (LNOI) or Silicon based devices are very attractive. For LNOI, a very recent implementation showed conversion efficiencies of 73% for pump powers of 260mW [95], although it suffers from the same noise sources as its non-integrated counterpart [96]. Silicon has a huge infrastructure behind it and is widely used in the integrated photonics world. QFC has been demonstrated in different types of waveguides like silicon nitride (SN_x) [97] or hydrogenated amorphous silicon (a-Si:H) [69], although their conversion efficiency and conversion bandwidth are not enough for our purposes. Probably the most promising concept is the silicon microring we already mentioned. By engineering the modes of a microresonator, one can produce QFC via Bragg Scattering while maintaining low dispersion and absorption rates. More than 60% efficiency over a large conversion bandwidth at less than 60 mW power of the pump beams has been demonstrated [71]. However, at this point of the investigations, the resultant noise if the pump is located at resonance makes the quantum conversion impossible, although it is mentioned that it would be possible to improve it by locating the high power pump in the signal band, instead of in the idler band.

The discussion of noise is of fundamental importance for quantum communication. A device with high noise will make difficult the collection of the converted photons or lower the fidelity of the entangled state ultimately destroying it. Therefore, numerous studies have been directed towards this topic. Usually, noise is measured in terms of the ratio between the power of light that has been converted to the wanted frequency, and that which has been generated at other frequencies. This is called signal-to-noise-ratio (SNR), and it is usually measured in dB as $SNR = 10 \log_{10}(P_{signal}/P_{noise})$. For periodically polled materials working with TWM processes, the main source of noise is the fabrication errors of the periodically polling, which results in low efficiency quasi-phase matching [98] and enhanced parasitic SPDC. Parasitic SPDC occurs when the intense pump beam doesn't interact with the signal photon but rather produces two photons with frequencies in the vicinity of our target wavelength, and it represents the biggest source of noise when the pump beam is far from the conversion wavelength [99, 100], which is likely our case. Nonetheless, When the pump beam is in the same band, the main source of noise is Raman Scattering¹⁴ [82], which will not be treated here. Another source of error can be cascaded TWM or Spontaneous FWM, but they are generally orders of magnitude lower. One detail to take into account is that noise counts usually grows linearly with

¹³Due to the fact that each pump is in a different band, resonant noise is largely suppressed.

¹⁴When a high power monochromatic beam penetrates a crystal, all the scattered light which does not have the same frequency as the initial beam is called Raman Scattering. If the frequencies are lower (higher), these components are called (anti-)Stokes components.

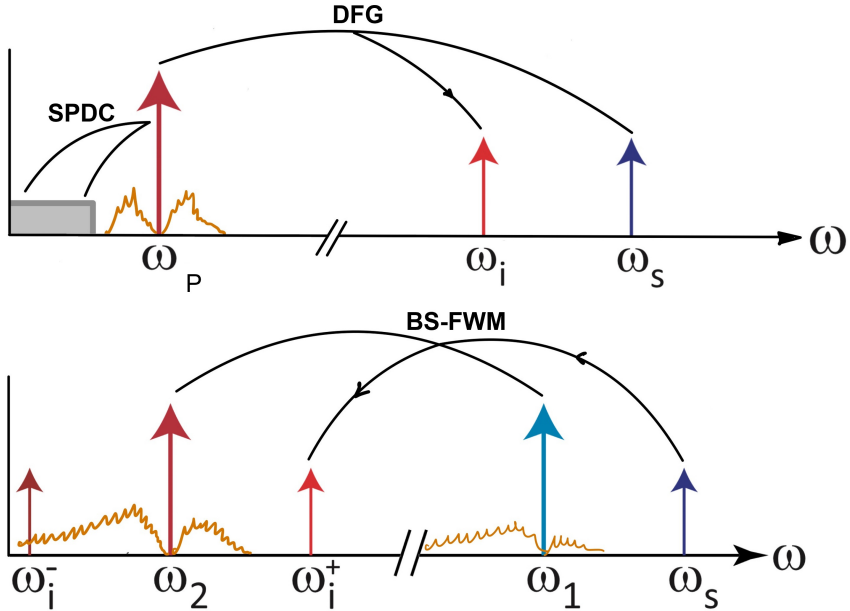


Figure 12: Possible implementations of QFC in our setup. The vertical axis is the relative intensity of each field, and the origin is arbitrary. The orange lines denote the noise produced by the pumps. The **top** figure shows the TWM configuration. On the left, we can see the noise plateau produced by parasitic SPDC of the pump (grey rectangle). The **bottom** figure shows the scheme for FWM. Here it is not represented, but it is not clear that the noise resulting from pump 1 will not affect the blue idler as it happens with the red idler.

pump power [100], so the conversion should be done at the lowest possible power.

On the other hand, the main source of error in FWM processes is the so-called two-photon absorption. As the name suggests, this is the absorption of two photons by the crystal which results in an excited state. Upon de-excitation, the atom or molecule can emit different types of broadband radiation¹⁵. Another important consideration is the still present Raman Scattering around the pumps. As in FWM the idlers are generated at the same distance of the second pump as the signal is from the first pump, it is important to choose a material which doesn't allow for resonances near 1550nm, and to position the second pump relatively far from the target conversion¹⁶ [71].

To conclude the QFC study, I include a diagram of the proposed characteristics for every type of conversion and the expected sources of noise.

In our specific case, our objective is to transform the 1092nm, or $\omega_s = 2\pi \times 274.72\text{THz}$, to the telecom band centred at 1550nm, i.e. $\omega_i = 2\pi \times 193.55\text{THz}$. If we hope to perform TWM, we have two options: either we put the pump as the higher energy beam ($\omega_i = \omega_p - \omega_s$) or we let it be the lower energy source ($\omega_i = \omega_s - \omega_p$). The first option produces more efficiency in the

¹⁵Normally, BS-FWM and TPA are competing processes, especially for the signal field. Under the presence of a strong pump beam in the signal band, TPA is greatly suppressed, but it is still non-negligible in the idler band [92].

¹⁶Although, the conversion efficiency is maximal when the pump-idler distance is minimal, as explained in the same reference.

conversion, but also results in noise orders of magnitude higher. By putting the pump at $3.7 \mu\text{m}$ ($\omega_P = 2\pi \times 81.08\text{THz}$), we highly reduce noise by Raman Scattering, because the pump is very far from the idler, and we avoid the parasitic SPDC noise plateau formed by the pump "fission" (see Figure 12) [77]. If instead we choose to proceed with FWM, we have several more options. Possibly the best is to allow the signal field to be the most energetic again, and take only the ω_i^+ field, similar to what is shown in [71], which could be achieved with $\omega_1 = 2\pi \times 260.87 \text{ Thz}$ (1150nm) and $\omega_2 = 2\pi \times 179.64\text{Thz}$ (1670nm). In this configuration, the ω_i^- field is rapidly washed away by TPA and Raman Scattering from the second pump, so we lose efficiency. Moreover, it is not clear that the noise from the first pump does not affect heavily our idler field, although it could be managed by putting more power in pump 2, as efficiency scales as the product of both powers [97].

5 Conclusion

During my short internship in the QITe group, I was able to interact in the frame of a Quantum Communication and Computation project. I took part in the design of a new setup for the collection of entangled photons capable of transmitting information between quantum memories, and I carried out a bibliographic study on the topic of Quantum Frequency Conversion that will help at the time to decide on how to move towards an optimal, efficient quantum network. For the future, the objective will be to optimise the new setup in order to be able to carry quantum state measurements that allow for setting a limit in the fidelity of the entanglement. Separate efforts will be needed to design and produce a QFC device from the information we have, to test it in our regime and conclude its utility. The final step will be joining both points of view, essentially generating long-range transmission of information, where the heralded entanglement of ions will be carried by frequency-converted photons. With an optimistic view, it is possible to imagine this technology being of revolutionary utility, not only in the communication and networking services but also as a way to scale up the awaited quantum computer, up to the limits of Quantum Supremacy.

A Ring Traps

Optical addressing of the ions and coherent control of the angular momentum state has been demonstrated in a similar setup [29,101], and an exhaustive description of the design can be found in [30,44]. In our setup, the RF electrodes produce a ring-shaped minimum of electrical potential located in a plane above the electrode surface. The DC electrodes are then configured to produce a minimum in one of the quarters of the ring. If we imagine the ring divided into four, looking from above, both photoionization lasers, the Doppler cooling laser and the repumper laser are all collimated and enter from the left. They are focused on the quarter where the RF electrodes set the minimum of the pseudo-potential, in order to ionise, trap and cool in the same site. Due to the symmetry of the trap, having a unique direction of absorption will produce the invisibility of the ions located in other sectors of the trap, which normally exist because the RF electrodes produce several minima of potential along the ring¹⁷. To avoid this, another Doppler cooling beam has been installed. This beam, however, has its shape modified by a cylindrical lens before entering the vacuum chamber, resulting in a rectangular-shaped beam that occupies the whole cross section of the trap. This beam also cools (contains the 422nm beam and the repumper beams) the ions and provides imaging to all places of the trap. An image of the trap and a scheme of the laser setup can be seen in Figure

¹⁷This could be unwanted but present due to construction imperfections on the trap, or because the electrodes are not well compensated.

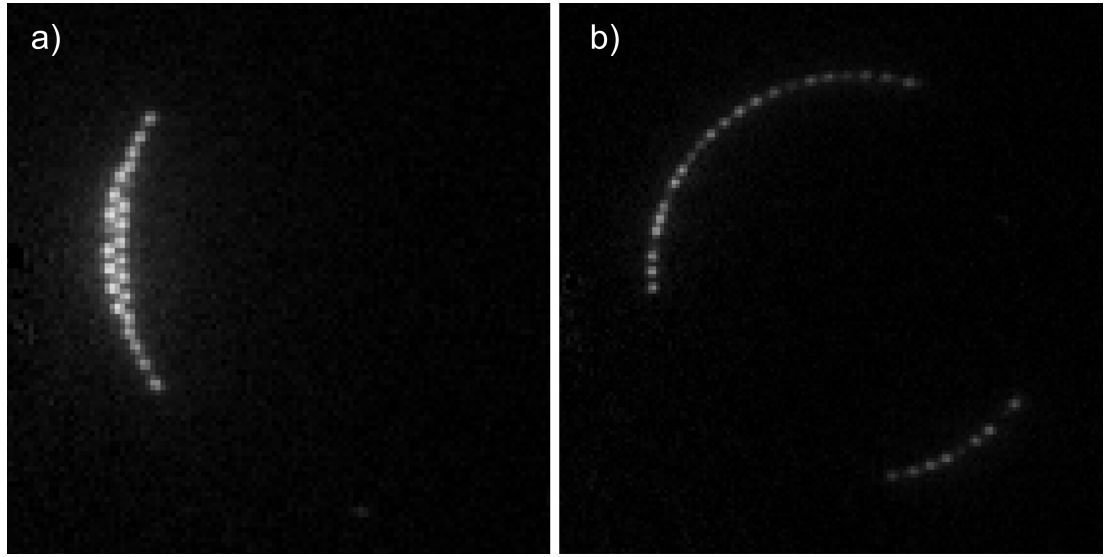


Figure 13: Ions captured in our setup. **a)** Pseudo-linear trap implemented in the ring by producing a strong minimum in the small section where the beams are tangential to the trap. The visible "zig-zag" configuration of the ions is an example of a quantum phase transition. **b)** In this case two minima are implemented (the top-right one more efficient than the one in the down-left quarter) and the ions are allowed to spread essentially forming one-dimensional chains.

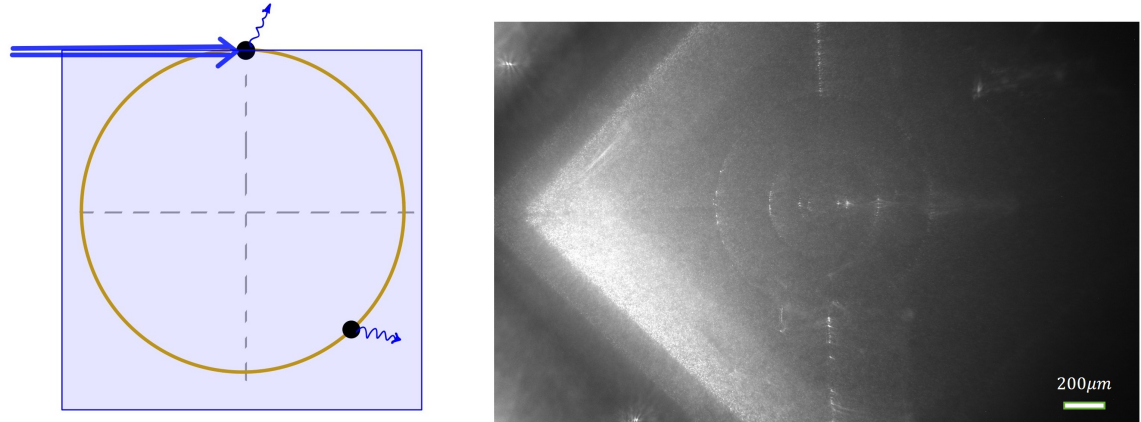


Figure 14: **Left**, a representation of our alignment of the lasers in the trap. The photoionisation, cooling and trapping are initially done in a chosen spot of the trap. The wide arrow indicates the incision of the co-propagating cooling and photoionising lasers, while the blue rectangle indicates a planar laser parallel to the trap, which contains not only the cooling but the IR repumpers too. This allows us to locate the ions throughout the whole ring trap. **Right**, a picture of our trap. Ions are trapped approximately $65\mu m$ above the first two circular electrodes. The scale is indicated in the bottom-right corner.

14. Figure 13.b shows the image of some ions trapped in our setup. Notice the presence of black spots between ions, which are actually ions of the less common isotopes $^{86}Sr^+$ and $^{87}Sr^{+18}$, which we cannot see because they do not fluoresce with the same light. The ring trap has a radius of 100 μm (although it can be varied by different designs of the electrodes) and can hold up to hundreds of atoms. As an extra, one interesting situation is depicted in Figure 13.a. When numerous ions are squashed together in a small section of the trap, the preferred minimal energy configuration is such that the ions rearrange in zigzag, essentially forming a triangular lattice. This configuration has been extensively studied in linear traps as an example of a quantum phase transition [102, 103]. From these images, much information can be extracted. For example, the distance between ions in the equilibrium position is directly related to the shape and strength of the potential well trapping the ions.

B Producing the ion-photon entanglement

In this Annex, I present a possible implementation of the whole pre-QFC experiment, starting from the photoionisation and cooling of ions inside the trap, to the actual entanglement procedure and needed manipulation of the ion qubit after the entanglement has happened, and finishing in the readout of the quantum state. A resume is presented in Figure 15, although an in-depth description of the sequence is available in this Annex.

An important point that we skipped in the main text due to reasons of space is the photoionisation of the Sr atoms. In our setup, Sr atoms are sublimated at a low rate from a very hot resistance. The photoionisation takes place in two steps, by two transitions at 461 and 405nm, leaving the atom in a self ionising final state [73]. These are intense beams that copropagate with the Doppler cooling beam and are focused in the intended position of the final ion, in a way that allows us to ionise, trap and cool in the same region of space. The first ionising beam, at 461nm, must have at least 1mW of power to saturate the $|5S_{1/2}\rangle \rightarrow |5P_{3/2}\rangle$ transition in the neutral Sr, while the secondary 405nm doesn't need so much power (around $100\mu W$ is enough) because the ionising transition is larger. The fact that Sr has a self ionising state that is easy to reach increases the ionising probability and is a huge advantage over other atoms which need far better stabilisation and intensity of the ionising beams.

The ions are Doppler cooled [36, 104, 105] by the blue 422nm laser¹⁹. This stage also requires the presence of a "repumper" beam, which empties the shelve states $|D_{3/2}\rangle$ and $|D_{5/2}\rangle$ that can get populated after the atom undergoes the Doppler cooling transition of 422nm. This is necessary for all atoms whose structure does not allow for Doppler cooling in a two level system. Essentially, if the atom relaxes to the $|D_{3/2}\rangle$ state from the excited $|P_{1/2}\rangle$, a repumper beam of 1003nm drives it to the second excited $|P_{3/2}\rangle$, from which it will decay back to the ground state with great probability. If instead the atom decays from $|P_{3/2}\rangle$ to the shelve state $|D_{5/2}\rangle$, then another repumper of 1033nm excites it back until the ground state is achieved. In the trapped ions team, they have developed a technique to measure the final temperature of these ions, finding for the Sr^+ ion a final temperature between 0.5 and 3 mK [37]

¹⁸There should be roughly 5 $^{88}Sr^+$ ions for each black spot, which can be checked in the figure.

¹⁹Contrarily to the case of neutral atoms and free ions, it is possible to cool a trapped ion in the 3 directions of space with the use of only one laser, provided that the beam is not parallel to any of the main directions of harmonic oscillations [106]

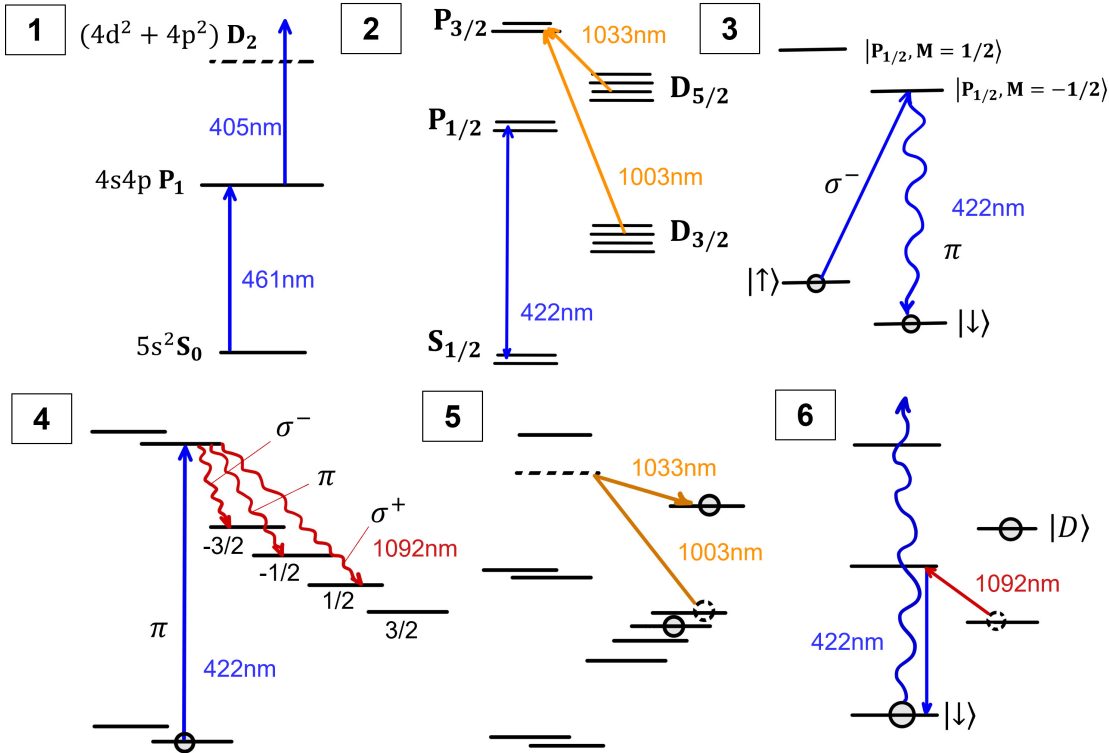


Figure 15: Stages of the ion-photon entanglement. The curvy lines designate a relaxation via spontaneous emission of a photon with the indicated polarization, while the straight lines are laser-driven transitions. **1.** The neutral Sr atom is photoionised in two stages, first is saturated in an excited state, and then excited towards a short-lived self ionising state (dashed line). **2.** The ion is Doppler cooled with the $|S_{1/2}\rangle \rightarrow |P_{1/2}\rangle$ transition (the laser detuning is not shown). Any possible transition to the $|D_{3/2}\rangle$ metastable state is repumped to the second excited state from which the state comes back to the ground state. **3.** Preparation of the ion in the $|\downarrow\rangle$ state. Any population in the $|\uparrow\rangle$ is pumped to the $|P_{1/2,-1/2}\rangle$ via a selective σ^- polarized beam that does not allow the state to go to any other level. The ion decays via a preferred π transition to our wanted initial state. **4.** Entanglement stage. The state is transferred to the $|D_{3/2}\rangle$ manifold, emitting a photon with the designated polarization in the way. In this stage, we discard the σ^+ polarized photons. **5.** One of the states in $|D_{3/2}\rangle$ is transferred to the $|D\rangle$ state via a dark resonance through a virtual level (dashed line) while leaving the other unaffected. This is managed by choosing a specific polarization in the 1003nm, but it is not indicated because several options are possible. **6.** Shelving readout stage. Connecting the cooling and the repumper laser we induce fluorescence only if the ion was not in the $|D\rangle$ state, allowing us to read the quantum state.

Another fundamental step is the preparation of the state before producing the entangled photons. The ion is, in principle, located in the ground state Zeeman basis. In order to be able to coherently transfer to the Zeeman manifold of $|D_{3/2}\rangle$, we need to select a specific transition for the cooling laser to have control over the entangled final states. Due to our present setup and the polarization options we have, the simplest case in transferring the population from the $|\downarrow\rangle$ state to the $|P_{1/2,-1/2}\rangle$ state

through a π pulse of 422nm from which the atom will decay with the Clebsch-Gordan coefficients indicated in equation 4. Therefore, all population must be prepared in the $|\downarrow\rangle$ state before starting the entangling sequence. For this, we use a σ^- polarized pump beam that connects the transition $|\uparrow\rangle \rightarrow |P_{1/2,-1/2}\rangle$, but none else. We apply this transition during 20 or 30 times the relaxation time back to $|\uparrow\rangle$ to ensure that no population is left there. In total, this "state preparation" stage takes around 200-300ns.

The metastable state, let us call it $|D_{3/2}\rangle \equiv |D'\rangle$, has 4 Zeeman levels connected to the $|P_{1/2}\rangle$ levels by the selection rules indicated in Figure 15. Once the atoms follow this transition, the ion and the photon will be in a superposition of three of these Zeeman levels, given by:

$$|\Psi\rangle = \frac{1}{\sqrt{2}}|m = -3/2, \sigma^-\rangle - \frac{1}{\sqrt{3}}|m = -1/2, \pi\rangle + \frac{1}{\sqrt{6}}|m = 1/2, \sigma^+\rangle \quad (4)$$

To be able to perform qubit operations, we essentially discard one of the three states, for example, the σ^+ because of it having the minimal probability of generation. We can do this by putting a polarizer in our detection scheme, in a way that, if this polarization is produced, the photon is not detected and the entanglement procedure is considered to have failed. This way, we essentially force the wavefunction to collapse towards the other two states.

This way, our photons are entangled with an ionic qubit in the $|D_{3/2}\rangle$ manifold. At this point, we can coherently transfer the population of one of the Zeeman states in the $|D_{3/2}\rangle$ manifold employing two distinct IR lasers, the same we use to repump in the Doppler stage. Therefore, in our case the "mapping" transition is done via a dark resonance between the three levels $|D_{3/2}\rangle \rightarrow |P_{3/2}\rangle \rightarrow |D_{5/2}\rangle$ that will ideally project the previous basis in $|D_{3/2}\rangle$ into an optical qubit where each state is in a different metastable $|D_{5/2}\rangle \equiv |D\rangle$ state²⁰. This shelving method depends on a dark resonance between the metastable levels $|D\rangle$ and $|D'\rangle$. This happens when the lasers connecting both levels to the $|P_{3/2}\rangle$ level are slightly detuned from such transition, but coincide in a transition on a virtual level²¹ [107]. The consequence is that the population transferred from $|D'\rangle$ passes through the virtual level directly into the $|D\rangle$ level, without coherent mapping to the $|P_{3/2}\rangle$ level itself. The existence of dark states has been long proven and many applications have been made regarding them in the Sr atom [108–110]. After this shelving, the state can be read applying the cooling 422nm and the 1092nm laser with the principle of shelving readout: if the ion was still in the $|D_{3/2}\rangle$ manifold, it will be pumped back to the first excited state and fluoresce. Another subtlety introduced by this method is that it modifies the fidelity of the entangled state. State-of-the-art ion-photon entanglement experiments report a fidelity in the range of 90-95% [111] and up to 98% [47, 112]. In our case, this fidelity will also depend on the fidelity of the coherent transfer of states. If this step is not optimised, the fidelity will be greatly reduced. In some experiments, coherent transfer is found to happen with 90% fidelity [107], which already makes us achieve only between only 88% overall fidelity in the best of cases.

A full sequence where we try to produce an entangled photon corresponds to stages 2, 3 and 4 on Figure 15. After the cooling of the ions, the preparation of the state is done by applying our polarization-dependent transition for 10-20 times the relaxation time of the transition $|P_{1/2,-1/2}\rangle \rightarrow |\uparrow\rangle$, to ensure that no population is left in the up-state. This takes around 200-300ns. Given the

²⁰Transferring only one of the Zeeman states in $|D_{3/2}\rangle$ is not trivial and free of errors. To be able to do this, we need very fine control of the polarization of the 1003nm laser connecting with the virtual level.

²¹In the context of Raman Scattering, a photon can be absorbed by the atom, exciting it to some energy state, even though such resonance doesn't exist. Energy is therefore not conserved in the process, but it is allowed by Heisenberg's uncertainty principle as long as the so called virtual level has a very short life.

AOM response time (around 50ns), a π pulse of such duration is implemented and then we wait 2-3 times the relaxation time of the transition, around 100ns, to ensure we do not stop the sequence before the photon gets emitted. Afterwards, we need to wait for an extra 100ns in case we detect an entangled photon for the electric signal to arrive at all devices stopping the sequence. The total time that a "try" cycle takes is around 750ns. Due to the branching ratio of the decay (5.8%), it takes 17 tries on average to obtain an entangled IR photon, and the ions need to be cooled again after 20-25 cycles, so we estimate a rate of 1 photon/20 cycles, which translates to 6.67×10^4 photons/second. For a maximum emission scenario, the objective only collects 4% of the total light emitted by the ion, due to their distance apart and the NA of the objective (solid angle collection), and the collective losses we estimated in the collection scheme, taking into account the objective, the dichroic and the fibre coupling, were around 9dB, meaning we essentially keep only 12.5% of the photons that enter the objective. Finally, we discard one of the entangled states and therefore we lose 1/6 of the first generated photons (see eq. 4). In summary, the number of entangled photons we can expect has an upper limit of:

$$N_{\text{photons}} = 6.67 * 10^4 \times 4\% \times 12.5\% \times 1/6 = 56 \text{ photons/second}$$

As a last step, one would need to know the efficiency of the single photon detector where the entangled photons are gonna be counted in the first stages of the experiment. With a first assumption of 50% (for superconducting single-photon detectors, the detection efficiency can be even higher), we already detect 28 photons/second, which is a great rate. This is a somewhat optimistic result, but that anyhow assures us that the project is feasible.

C Manipulation and characterization of optical fibres

During the beginning of my internship, I learnt how to cleave and splice optic fibres with the objective to repair the optic lines connecting the photonics and trapped ions laboratories. A colleague and I developed a consistent way to peel the fibres and splice them with the device *EasySplicer MK2*, and we wrote a series of instructions that remain in the Trapped Ions internal blog in case another reparation is needed. My contribution to these guidelines were the pictures, the schematic drawings and part of the text. The sheet can be found [here](#).

References

- [1] Jonathan P Dowling and Gerard J Milburn. Quantum technology: the second quantum revolution. *Philosophical Transactions of the Royal Society of London. Series A: Mathematical, Physical and Engineering Sciences*, 361(1809):1655–1674, 2003.
- [2] David Deutsch. Quantum theory, the church–turing principle and the universal quantum computer. *Proceedings of the Royal Society of London. A. Mathematical and Physical Sciences*, 400(1818):97–117, 1985.
- [3] Richard P Feynman. Simulating physics with computers. In *Feynman and computation*, pages 133–153. CRC Press, 2018.
- [4] Peter W Shor. Algorithms for quantum computation: discrete logarithms and factoring. In *Proceedings 35th annual symposium on foundations of computer science*, pages 124–134. Ieee, 1994.

- [5] Mirko Amico, Zain H Saleem, and Muir Kumph. Experimental study of shor's factoring algorithm using the ibm q experience. *Physical Review A*, 100(1):012305, 2019.
- [6] Peter JJ O'Malley, Ryan Babbush, Ian D Kivlichan, Jonathan Romero, Jarrod R McClean, Rami Barends, Julian Kelly, Pedram Roushan, Andrew Tranter, Nan Ding, et al. Scalable quantum simulation of molecular energies. *Physical Review X*, 6(3):031007, 2016.
- [7] M Evers, A Heid, and E Ostojic. Pharma's digital rx: Quantum computing in drug research and development, 2021.
- [8] Iulia M Georgescu, Sahel Ashhab, and Franco Nori. Quantum simulation. *Reviews of Modern Physics*, 86(1):153, 2014.
- [9] David Kielpinski, Chris Monroe, and David J Wineland. Architecture for a large-scale ion-trap quantum computer. *Nature*, 417(6890):709–711, 2002.
- [10] Christopher Monroe and Jungsang Kim. Scaling the ion trap quantum processor. *Science*, 339(6124):1164–1169, 2013.
- [11] Marco Tomamichel and Anthony Leverrier. A largely self-contained and complete security proof for quantum key distribution. *Quantum*, 1:14, 2017.
- [12] C. E. Shannon. Communication theory of secrecy systems. *The Bell System Technical Journal*, 28(4):656–715, 1949.
- [13] Dik Bouwmeester, Jian-Wei Pan, Klaus Mattle, Manfred Eibl, Harald Weinfurter, and Anton Zeilinger. Experimental quantum teleportation. *Nature*, 390(6660):575–579, 1997.
- [14] Charles H. Bennett, Gilles Brassard, Claude Crépeau, Richard Jozsa, Asher Peres, and William K. Wootters. Teleporting an unknown quantum state via dual classical and einstein-podolsky-rosen channels. *Phys. Rev. Lett.*, 70:1895–1899, Mar 1993.
- [15] H Jeff Kimble. The quantum internet. *Nature*, 453(7198):1023–1030, 2008.
- [16] Jing Tao, Jean-Pierre Likforman, Peng Zhao, Hong Yu Li, Theo Henner, Yu Dian Lim, Wen Wei Seit, Luca Guidoni, and Chuan Seng Tan. Large-scale fabrication of surface ion traps on a 300 mm glass wafer. *physica status solidi (b)*, 258(7):2000589, 2021.
- [17] Peng Zhao, JP Likforman, Hong Yu Li, Jing Tao, T Henner, Yu Dian Lim, WW Seit, Chuan Seng Tan, and Luca Guidoni. Tsv-integrated surface electrode ion trap for scalable quantum information processing. *Applied Physics Letters*, 118(12):124003, 2021.
- [18] Boris B Blinov, David L Moehring, L-M Duan, and Chris Monroe. Observation of entanglement between a single trapped atom and a single photon. *Nature*, 428(6979):153–157, 2004.
- [19] David Hucul, Ismail V Inlek, Grahame Vittorini, Clayton Crocker, Shantanu Debnath, Susan M Clark, and Christopher Monroe. Modular entanglement of atomic qubits using photons and phonons. *Nature Physics*, 11(1):37–42, 2015.
- [20] Jungsang Kim, Peter Maunz, Taehyun Kim, Jeffrey Hussman, Rachel Noek, Abhijit Mehta, and Christopher Monroe. Modular universal scalable ion-trap quantum computer (musiqc). In *AIP Conference Proceedings*, volume 1363, pages 190–193. American Institute of Physics, 2011.

- [21] P Drmota, D Main, DP Nadlinger, BC Nichol, MA Weber, EM Ainley, A Agrawal, R Srinivas, G Araneda, CJ Ballance, et al. Robust quantum memory in a trapped-ion quantum network node. *arXiv preprint arXiv:2210.11447*, 2022.
- [22] G. P. Agrawal. *Nonlinear Fiber Optics*. Academic Press, 2007.
- [23] W Jones. Earnshaw's theorem and the stability of matter. *European Journal of Physics*, 1(2):85, 1980.
- [24] Wolfgang Paul. Electromagnetic traps for charged and neutral particles (nobel lecture). *Angewandte Chemie International Edition in English*, 29(7):739–748, 1990.
- [25] Benjamin Szymanski. *Piégeage et refroidissement d'ions strontium dans des pièges microfabriqués*. PhD thesis, UNIVERSITÉ PARIS DIDEROT (Paris 7) SORBONNE PARIS CITE, 2013.
- [26] JD Prestage, Go J Dick, and L Maleki. New ion trap for frequency standard applications. *Journal of Applied Physics*, 66(3):1013–1017, 1989.
- [27] Marissa D'Onofrio, Yuanheng Xie, AJ Rasmussen, Evangeline Wolanski, Jiafeng Cui, and Philip Richerme. Radial two-dimensional ion crystals in a linear paul trap. *Physical Review Letters*, 127(2):020503, 2021.
- [28] K Okada, M Wada, T Takayanagi, S Ohtani, and HA Schuessler. Characterization of ion coulomb crystals in a linear paul trap. *Physical Review A*, 81(1):013420, 2010.
- [29] Hao-Kun Li, Erik Urban, Crystal Noel, Alexander Chuang, Yang Xia, Anthony Ransford, Boerge Hemmerling, Yuan Wang, Tongcang Li, Hartmut Häffner, et al. Achieving translational symmetry in trapped cold ion rings. *arXiv preprint arXiv:1605.02143*, 2016.
- [30] John Chiaverini, R Brad Blakestad, Joe Britton, John D Jost, Chris Langer, Dietrich Leibfried, Roe Ozeri, and David J Wineland. Surface-electrode architecture for ion-trap quantum information processing. *arXiv preprint quant-ph/0501147*, 2005.
- [31] Signe Seidelin, John Chiaverini, Rainer Reichle, John J Bollinger, Didi Leibfried, Joe Britton, JH Wesenberg, RB Blakestad, RJ Epstein, DB Hume, et al. Microfabricated surface-electrode ion trap for scalable quantum information processing. *Physical review letters*, 96(25):253003, 2006.
- [32] Juan I Cirac and Peter Zoller. Quantum computations with cold trapped ions. *Physical review letters*, 74(20):4091, 1995.
- [33] Philipp Schindler, Daniel Nigg, Thomas Monz, Julio T Barreiro, Esteban Martinez, Shannon X Wang, Stephan Quint, Matthias F Brandl, Volckmar Nebendahl, Christian F Roos, et al. A quantum information processor with trapped ions. *New Journal of Physics*, 15(12):123012, 2013.
- [34] Karan K Mehta, Colin D Bruzewicz, Robert McConnell, Rajeev J Ram, Jeremy M Sage, and John Chiaverini. Integrated optical addressing of an ion qubit. *Nature nanotechnology*, 11(12):1066–1070, 2016.
- [35] M Ivory, WJ Setzer, N Karl, H McGuinness, C DeRose, M Blain, D Stick, M Gehl, and LP Parazzoli. Integrated optical addressing of a trapped ytterbium ion. *Physical Review X*, 11(4):041033, 2021.

- [36] Jürgen Eschner, Giovanna Morigi, Ferdinand Schmidt-Kaler, and Rainer Blatt. Laser cooling of trapped ions. *JOSA B*, 20(5):1003–1015, 2003.
- [37] Vincent Tugayé, Jean-Pierre Likforman, Samuel Guibal, and Luca Guidoni. Absolute single-ion thermometry. *Physical Review A*, 99(2):023412, 2019.
- [38] Jan Benhelm, Gerhard Kirchmair, Christian F Roos, and Rainer Blatt. Towards fault-tolerant quantum computing with trapped ions. *Nature Physics*, 4(6):463–466, 2008.
- [39] Karan K Mehta, Chi Zhang, Maciej Malinowski, Thanh-Long Nguyen, Martin Stadler, and Jonathan P Home. Integrated optical multi-ion quantum logic. *Nature*, 586(7830):533–537, 2020.
- [40] Mark Webber, Vincent Elfving, Sebastian Weidt, and Winfried K Hensinger. The impact of hardware specifications on reaching quantum advantage in the fault tolerant regime. *AVS Quantum Science*, 4(1):013801, 2022.
- [41] Andrew D King, Jack Raymond, Trevor Lanting, Richard Harris, Alex Zucca, Fabio Altomare, Andrew J Berkley, Kelly Boothby, Sara Ejtemaei, Colin Enderud, et al. Quantum critical dynamics in a 5,000-qubit programmable spin glass. *Nature*, pages 1–6, 2023.
- [42] Sheir Yarkoni, Elena Raponi, Thomas Bäck, and Sebastian Schmitt. Quantum annealing for industry applications: Introduction and review. *Reports on Progress in Physics*, 2022.
- [43] Pengfei Wang, Chun-Yang Luan, Mu Qiao, Mark Um, Junhua Zhang, Ye Wang, Xiao Yuan, Mile Gu, Jingning Zhang, and Kihwan Kim. Single ion qubit with estimated coherence time exceeding one hour. *Nature communications*, 12(1):233, 2021.
- [44] Po-Jen Wang, Tongcang Li, Crystal Noel, Xiang Zhang, and Hartmut Häffner. Design of a surface trap for freely rotating ion ring crystals. *arXiv preprint arXiv:1412.3551*, 2014.
- [45] Laurent Stephenson. *Entanglement between nodes of a quantum network*. PhD thesis, University of Oxford, 2019.
- [46] Dana J Berkeland. Quantum information with trapped strontium ions. *Los Alamos Science*, 27:178–183, 2002.
- [47] LJ Stephenson, DP Nadlinger, BC Nichol, S An, P Drmota, TG Ballance, K Thirumalai, JF Goodwin, DM Lucas, and CJ Ballance. High-rate, high-fidelity entanglement of qubits across an elementary quantum network. *Physical review letters*, 124(11):110501, 2020.
- [48] Vincent Tugaye. *Spectroscopie et thermométrie d'ions uniques $^{88}\text{Sr}^+$ capturés dans des micropièges surfaciques aspects théoriques et expérimentaux*. PhD thesis, Université Paris Cité, 2020.
- [49] Tomokazu Kogure and Kam-Ching Leung. *The astrophysics of emission-line stars*, volume 342. Springer Science & Business Media, 2010.
- [50] Alain Aspect, Philippe Grangier, and Gérard Roger. Experimental tests of realistic local theories via bell's theorem. *Phys. Rev. Lett.*, 47:460–463, Aug 1981.

- [51] GB Xavier, Nino Walenta, G Vilela de Faria, GP Temporão, Nicolas Gisin, Hugo Zbinden, and Jean-Pierre Von Der Weid. Experimental polarization encoded quantum key distribution over optical fibres with real-time continuous birefringence compensation. *New Journal of Physics*, 11(4):045015, 2009.
- [52] Daniel Barbosa de Brito, JosÉ ClÁudio do Nascimento, and Rubens Viana Ramos. Quantum communication with polarization-encoded qubit using quantum error correction. *IEEE Journal of Quantum Electronics*, 44(2):113–118, 2008.
- [53] Shan W Jolin, Gustav Andersson, JC Rivera Hernández, Ingrid Strandberg, Fernando Quijandría, José Aumentado, Riccardo Borgani, Mats O Tholén, and David B Haviland. Multipartite entanglement in a microwave frequency comb. *Physical Review Letters*, 130(12):120601, 2023.
- [54] Jihua Zhang, Jinyong Ma, Matthew Parry, Marcus Cai, Rocio Camacho-Morales, Lei Xu, Dragomir N Neshev, and Andrey A Sukhorukov. Spatially entangled photon pairs from lithium niobate nonlocal metasurfaces. *Science Advances*, 8(30):eabq4240, 2022.
- [55] Jürgen Brendel, Nicolas Gisin, Wolfgang Tittel, and Hugo Zbinden. Pulsed energy-time entangled twin-photon source for quantum communication. *Physical Review Letters*, 82(12):2594, 1999.
- [56] Michael A Nielsen and Isaac Chuang. Quantum computation and quantum information, 2002.
- [57] Saverio Francesconi. *On-chip generation of high-dimensional entangled states of light*. PhD thesis, Université Paris Cité, 2020.
- [58] Robert W Boyd. *Nonlinear optics*. Academic press, 2020.
- [59] Rikizo Ikuta, Yoshiaki Kusaka, Tsuyoshi Kitano, Hiroshi Kato, Takashi Yamamoto, Masato Koashi, and Nobuyuki Imoto. Wide-band quantum interface for visible-to-telecommunication wavelength conversion. *Nature communications*, 2(1):537, 2011.
- [60] Sara Ducci, Perola Milman, and Eleni Diamanti. Generation of quantum states of light in nonlinear algaas chips: engineering and applications. *Photoniques*, (107):28–34, 2021.
- [61] Félicien Appas, Othmane Meskine, Aristide Lemaître, José Palomo, Florent Baboux, Maria I Amanti, and Sara Ducci. Broadband biphoton generation and polarization splitting in a monolithic algaas chip. *ACS Photonics*, 10(4):1136–1143, 2023.
- [62] Roger Stolen and John Bjorkholm. Parametric amplification and frequency conversion in optical fibers. *IEEE Journal of Quantum Electronics*, 18(7):1062–1072, 1982.
- [63] Jonas Hansryd, Peter A Andrekson, Mathias Westlund, Jie Li, and P-O Hedekvist. Fiber-based optical parametric amplifiers and their applications. *IEEE Journal of Selected Topics in Quantum Electronics*, 8(3):506–520, 2002.
- [64] H Pakarzadeh and A Zakery. Investigation of two-pump fiber optical parametric amplifiers for a broadband and flat gain with a low pump-to-signal noise transfer. *Journal of Nonlinear Optical Physics & Materials*, 24(03):1550038, 2015.
- [65] S Radic and CJ McKinstry. Two-pump fiber parametric amplifiers. *Optical Fiber Technology*, 9(1):7–23, 2003.

- [66] CJ McKinstrie, JD Harvey, S Radic, and MG Raymer. Translation of quantum states by four-wave mixing in fibers. *Optics Express*, 13(22):9131–9142, 2005.
- [67] Amnon Yariv, Dan Fekete, and David M Pepper. Compensation for channel dispersion by nonlinear optical phase conjugation. *Optics Letters*, 4(2):52–54, 1979.
- [68] Karen Solis-Trapala, Takashi Inoue, and Shu Namiki. Nearly-ideal optical phase conjugation based nonlinear compensation system. In *Optical Fiber Communication Conference*, pages W3F–8. Optica Publishing Group, 2014.
- [69] Kangmei Li, Hongcheng Sun, and Amy C Foster. Four-wave mixing bragg scattering in hydrogenated amorphous silicon waveguides. *Optics letters*, 42(8):1488–1491, 2017.
- [70] L Mejling, CJ McKinstrie, MG Raymer, and K Rottwitt. Quantum frequency translation by four-wave mixing in a fiber: low-conversion regime. *Optics Express*, 20(8):8367–8396, 2012.
- [71] Qing Li, Marcelo Davanço, and Kartik Srinivasan. Efficient and low-noise single-photon-level frequency conversion interfaces using silicon nanophotonics. *Nature Photonics*, 10(6):406–414, 2016.
- [72] Paveen Apiratikul, Jeremiah J Wathen, Gyorgy A Porkolab, Bohan Wang, Lei He, Thomas E Murphy, and Christopher JK Richardson. Enhanced continuous-wave four-wave mixing efficiency in nonlinear algaas waveguides. *Optics express*, 22(22):26814–26824, 2014.
- [73] Sébastien Removille. *VERS UNE MEMOIRE QUANTIQUE AVEC DES IONS PIEGES*. Theses, Université Paris-Diderot - Paris VII, September 2009.
- [74] V Jacques, B Hingant, A Allafort, M Pigeard, and JF Roch. Nonlinear spectroscopy of rubidium: an undergraduate experiment. *European journal of physics*, 30(5):921, 2009.
- [75] Florian Kaiser, Panagiotis Vergyris, Anthony Martin, Djeylan Aktas, Marc P De Michelis, Olivier Alibart, and Sébastien Tanzilli. Quantum optical frequency up-conversion for polarisation entangled qubits: towards interconnected quantum information devices. *Optics Express*, 27(18):25603–25610, 2019.
- [76] Anaës Dréau, Anna Tchepotareva, Aboubakr El Mahdaoui, Cristian Bonato, and Ronald Hanson. Quantum frequency conversion of single photons from a nitrogen-vacancy center in diamond to telecommunication wavelengths. *Physical review applied*, 9(6):064031, 2018.
- [77] Vahid Esfandyarpour, Carsten Langrock, and Martin Fejer. Cascaded downconversion interface to convert single-photon-level signals at 650 nm to the telecom band. *Optics Letters*, 43(22):5655–5658, 2018.
- [78] Beatrice Da Lio, Carlos Faurby, Xiaoyan Zhou, Ming Lai Chan, Ravitej Uppu, Henri Thyrrstrup, Sven Scholz, Andreas D Wieck, Arne Ludwig, Peter Lodahl, et al. A pure and indistinguishable single-photon source at telecommunication wavelength. *Advanced Quantum Technologies*, 5(5):2200006, 2022.
- [79] Sebastian Zaske, Andreas Lenhard, and Christoph Becher. Efficient frequency downconversion at the single photon level from the red spectral range to the telecommunications c-band. *Optics express*, 19(13):12825–12836, 2011.

- [80] Jason S Pelc, Lijun Ma, CR Phillips, Qiang Zhang, C Langrock, Oliver Slattery, Xiao Tang, and Martin M Fejer. Long-wavelength-pumped upconversion single-photon detector at 1550 nm: performance and noise analysis. *Optics express*, 19(22):21445–21456, 2011.
- [81] Benjamin Kambs, Jan Kettler, Matthias Bock, Jonas Nils Becker, Carsten Arend, Andreas Lenhard, Simone Luca Portalupi, Michael Jetter, Peter Michler, and Christoph Becher. Low-noise quantum frequency down-conversion of indistinguishable photons. *Optics express*, 24(19):22250–22260, 2016.
- [82] Carsten Langrock, Eleni Diamanti, Rostislav V Roussev, Yoshihisa Yamamoto, Martin M Fejer, and Hiroki Takesue. Highly efficient single-photon detection at communication wavelengths by use of upconversion in reverse-proton-exchanged periodically poled linbo 3 waveguides. *Optics letters*, 30(13):1725–1727, 2005.
- [83] Sergey Gagarskiy, Sergey Grechin, Pioter Druzhinin, Kiyoshi Kato, David Kochiev, Pavel Nikolaev, and Nobihuro Umemura. Frequency conversion in ktp crystal and its isomorphs. *Crystals*, 8(10):386, 2018.
- [84] YS Chen, SW Tsai, SS Wang, and YF Chen. Diode-pumped q-switched yellow laser with single-pass sum-frequency mixing: comparison between ppln and ppktp. In *CLEO/Pacific Rim 2003. The 5th Pacific Rim Conference on Lasers and Electro-Optics (IEEE Cat. No. 03TH8671)*, volume 2, pages 491–vol. IEEE, 2003.
- [85] Carlota Canalias, Junji Hirohashi, Valdas Pasiskevicius, and Fredrik Laurell. Polarization-switching characteristics of flux-grown $\text{K}_\text{Ti}\text{OPO}_4$ and $\text{Rb}_\text{Ti}\text{OPO}_4$ at room temperature. *Journal of applied physics*, 97(12):124105, 2005.
- [86] Patrick Mutter, Andrius Zukauskas, and Carlota Canalias. Domain dynamics in coercive-field engineered sub- μm periodically poled rb-doped KTiOPO_4 . *Optical Materials Express*, 12(11):4332–4340, 2022.
- [87] Kjell Martin Mølster. *Backward and Forward Nonlinear Optical Processes in Potassium Titanyl Phosphate*. PhD thesis, KTH Royal Institute of Technology, 2023.
- [88] Felix Mann, Felipe Gewers, Marlon Placke, Helen M Chrzanowski, and Sven Ramelow. Low-noise quantum frequency conversion in a monolithic bulk ppktp cavity. *arXiv preprint arXiv:2304.13459*, 2023.
- [89] Z Vernon, M Liscidini, and JE Sipe. Quantum frequency conversion and strong coupling of photonic modes using four-wave mixing in integrated microresonators. *Physical Review A*, 94(2):023810, 2016.
- [90] Chin-Yao Cheng, Jia-Juan Lee, Zi-Yu Liu, Jiun-Shiuan Shiu, and Yong-Fan Chen. Quantum frequency conversion based on resonant four-wave mixing. *Physical Review A*, 103(2):023711, 2021.
- [91] Eyal Bahar, Xiaoyue Ding, Asaf Dahan, Haim Suchowski, and Jeffrey Moses. Adiabatic four-wave mixing frequency conversion. *Optics Express*, 26(20):25582–25601, 2018.
- [92] Prathamesh S Donvalkar, Vivek Venkataraman, Stéphane Clemmen, Kasturi Saha, and Alexander L Gaeta. Frequency translation via four-wave mixing bragg scattering in rb filled photonic bandgap fibers. *Optics letters*, 39(6):1557–1560, 2014.

- [93] Kyo Inoue. Tunable and selective wavelength conversion using fiber four-wave mixing with two pump lights. *IEEE photonics technology letters*, 6(12):1451–1453, 1994.
- [94] Z Vernon and JE Sipe. Strongly driven nonlinear quantum optics in microring resonators. *Physical Review A*, 92(3):033840, 2015.
- [95] Xina Wang, Xufeng Jiao, Bin Wang, Yang Liu, Xiu-Ping Xie, Ming-Yang Zheng, Qiang Zhang, and Jian-Wei Pan. Quantum frequency conversion and single-photon detection with lithium niobate nanophotonic chips. *npj Quantum Information*, 9(1):38, 2023.
- [96] Heng Fan, Zhaohui Ma, Jiayang Chen, Zhan Li, Chao Tang, Yong Meng Sua, and Yuping Huang. Photon conversion in thin-film lithium niobate nanowaveguides: a noise analysis. *JOSA B*, 38(7):2172–2179, 2021.
- [97] Imad Agha, Serkan Ates, Marcelo Davanço, and Kartik Srinivasan. A chip-scale, telecommunications-band frequency conversion interface for quantum emitters. *Optics express*, 21(18):21628–21638, 2013.
- [98] Jason S Pelc, Carsten Langrock, Qiang Zhang, and Martin M Fejer. Influence of domain disorder on parametric noise in quasi-phase-matched quantum frequency converters. *Optics letters*, 35(16):2804–2806, 2010.
- [99] Marius A Albota and Franco NC Wong. Efficient single-photon counting at $1.55 \mu\text{m}$ by means of frequency upconversion. *Optics letters*, 29(13):1449–1451, 2004.
- [100] Peter C Strassmann, Anthony Martin, Nicolas Gisin, and Mikael Afzelius. Spectral noise in frequency conversion from the visible to the telecommunication c-band. *Optics express*, 27(10):14298–14307, 2019.
- [101] Erik Urban, Neil Glikin, Sara Mouradian, Kai Krimmel, Boerge Hemmerling, and Hartmut Haeffner. Coherent control of the rotational degree of freedom of a two-ion coulomb crystal. *Physical review letters*, 123(13):133202, 2019.
- [102] Efrat Shimshoni, Giovanna Morigi, and Shmuel Fishman. Quantum zigzag transition in ion chains. *Physical review letters*, 106(1):010401, 2011.
- [103] A Retzker, RC Thompson, DM Segal, and MB Plenio. Double well potentials and quantum phase transitions in ion traps. *Physical review letters*, 101(26):260504, 2008.
- [104] Stig Stenholm. The semiclassical theory of laser cooling. *Reviews of modern physics*, 58(3):699, 1986.
- [105] Theodor W Hänsch and Arthur L Schawlow. Cooling of gases by laser radiation. *Optics Communications*, 13(1):68–69, 1975.
- [106] Wayne M Itano and DJ Wineland. Laser cooling of ions stored in harmonic and penning traps. *Physical Review A*, 25(1):35, 1982.
- [107] MJ McDonnell, J-P Stacey, SC Webster, JP Home, A Ramos, DM Lucas, DN Stacey, and AM Steane. High-efficiency detection of a single quantum of angular momentum by suppression of optical pumping. *Physical review letters*, 93(15):153601, 2004.

- [108] Kurt R Vogel, Tim P Dinneen, Alan C Gallagher, and John L Hall. Experiments with strontium in a vapor cell magneto-optic trap. In *Methods for Ultrasensitive Detection*, volume 3270, pages 77–84. SPIE, 1998.
- [109] Matthew N Winchester, Matthew A Norcia, Julia RK Cline, and James K Thompson. Magnetically induced optical transparency on a forbidden transition in strontium for cavity-enhanced spectroscopy. *Physical Review Letters*, 118(26):263601, 2017.
- [110] Adam L Shaw, Pascal Scholl, Ran Finklestein, Ivaylo S Madjarov, Brandon Grinkemeyer, and Manuel Endres. Dark-state enhanced loading of an optical tweezer array. *Physical Review Letters*, 130(19):193402, 2023.
- [111] John Hannegan, James D Siversns, and Qudsia Quraishi. Entanglement between a trapped-ion qubit and a 780-nm photon via quantum frequency conversion. *Physical Review A*, 106(4):042441, 2022.
- [112] Matthias Bock, Stephan Kucera, Pascal Eich, Matthias Kreis, Andreas Lenhard, Jürgen Eschner, and Christoph Becher. Polarization-preserving quantum frequency conversion for entanglement distribution in trapped-atom based quantum networks. In *Quantum Information and Measurement*, pages T5A–74. Optica Publishing Group, 2019.